Design Optimization of Multi–Element High–Lift Configurations Using a Viscous Continuous Adjoint Method

Sangho Kim*, Juan J. Alonso†, and Antony Jameson‡

Stanford University, Stanford, CA 94305

ABSTRACT

An adjoint-based Navier-Stokes design and optimization method for two-dimensional multi-element high-lift configurations is derived and presented. The compressible Reynolds-Averaged Navier-Stokes equations are used as a flow model together with the Spalart-Allmaras turbulence model to account for high Reynolds number effects. Using a viscous continuous adjoint formulation, the necessary aerodynamic gradient information is obtained with large computational savings over traditional finite-difference methods. The high-lift configuration parallel design method uses a point-to-point matched multi-block grid system and the Message Passing Interface standard for communication in both the flow and adjoint calculations. Airfoil shape, element positioning, and angle of attack are used as design variables. The prediction of high-lift flows around a baseline three-element airfoil configuration, denoted as 30P30N, is validated by comparison with available experimental data. Finally, several design results that verify the potential of the method for high-

*Postdoctoral Scholar, Department of Aeronautics and Astronautics, Stanford University

†Assistant Professor, Department of Aeronautics and Astronautics, Stanford University, AIAA Member

‡Thomas V. Jones Professor of Engineering, Department of Aeronautics and Astronautics, Stanford University, AIAA Fellow

lift system design and optimization, are presented. The design examples include a multi-element inverse design problem and the following optimization problems: lift coefficient maximization, lift-to-drag ratio maximization, and the maximum lift coefficient maximization problem for both the RAE2822 single-element airfoil and the 30P30N multi-element airfoil.

NOMENCLATURE

c	=	chord length
C_d, C_l	=	airfoil coefficients of drag and lift
$C_{l_{max}}$	=	maximum lift coefficient
C_p	=	pressure coefficient
$C_{p_{crt}}$	=	critical pressure coefficient
D	=	drag
t/c	=	thickness-to-chord ratio
$\mathcal{F}$	=	boundary shape
$\mathcal{G}$	=	gradient vector
H	=	total enthalpy
I	=	cost function
L	=	lift
M_∞	=	free stream Mach number
p	=	static pressure
p_d	=	desired target static pressure
R	=	governing equations or residual
Re	=	Reynolds number
S	=	surface area
w	=	conservative flow variables in Cartesian coordinates
x,y	=	Cartesian coordinates
y^+	=	dimensionless wall distance
α	=	angle of attack
α_{clmax}	=	stall angle of attack
δ	=	first variation
λ	=	step size in steepest descent method
ψ	=	Lagrange multiplier, co-state or adjoint variable

INTRODUCTION

Aerodynamic shape design has long been a challenging objective in the study of fluid dynamics. Computational Fluid Dynamics (CFD) has played an important analysis role in the aerodynamic design process since its introduction. However, CFD has been mostly used in the analysis of aerodynamic configurations in order to aid in the design process rather than to serve as a direct design tool in aerodynamic shape optimization. Although several attempts have been made in the past to use CFD as a direct design tool [1,2,3,4,5], it has not been until recently that the focus of CFD applications has shifted to aerodynamic design [6,7,8,9,10,11]. This shift has been mainly motivated by the availability of high performance computing platforms and by the development of new and efficient analysis and design algorithms. In particular, automatic design procedures which use CFD combined with gradient-based optimization techniques have made it possible to remove difficulties in the decision making process faced by the applied aerodynamicist.

In gradient-based optimization methods, finding a fast and accurate way of calculating the necessary gradient information is essential to developing an effective design method since this can be the most time consuming portion of the design algorithm. Gradient information can be computed using a variety of approaches, such as the finite-difference method, the complex-step method [12] and automatic differentiation [13]. Unfortunately, except for the case of the *reverse mode* of automatic differentiation, their computational cost is proportional to the number of design variables in the problem, which can be rather large.

An alternative choice, the control theory approach, has dramatic computational cost and storage advantages when compared to any of these methods. The foundation of control theory for systems governed by partial differential equations was laid by Lions [14]. The control theory approach is often called the adjoint method, since the necessary gradients are obtained via the solution of the adjoint equations of the governing equations of interest. The adjoint method is extremely efficient

since the computational expense incurred in the calculation of the complete gradient is effectively *independent* of the number of design variables. The only cost involved is the calculation of *one* flow solution and *one* adjoint solution whose complexity is similar to that of the flow solution. Control theory was applied in this way to shape design for elliptic equations by Pironneau [15] and it was first used in transonic flow by Jameson [6,7,16]. Since then, this method has become a popular choice for design problems involving fluid flow [9,17,18,19].

Most of the early work in the formulation of the adjoint-based design framework used the potential and Euler equations as models of the fluid flow. Aerodynamic design calculations using the Reynolds-Averaged Navier-Stokes equations as the flow model have only recently been tackled. In 1997, a continuous adjoint method for Aerodynamic Shape Optimization (ASO) using the compressible Navier-Stokes equations was formulated and it has been implemented directly in a three-dimensional wing problem [16,20]. Since these design calculations were carried out without the benefit of a careful check of the accuracy of the resulting gradient information, a series of numerical experiments in two dimensions were conducted by the authors [21] to determine the validity of the results. Existing approaches to the adjoint method can be classified into two categories: the *continuous* adjoint and *discrete* adjoint methods. If the adjoint equations are directly derived from the governing equations and then discretized, they are termed *continuous*, while if, instead, they are directly derived from the discretized form of the governing equations they are referred to as *discrete*. In theory, the *discrete* adjoint method should give gradients which are closer in value to exact finite-difference gradients. On the other hand, the *continuous* adjoint method has the advantage that the adjoint system has a unique form independent of the scheme used to solve the flow-field system. Nadarajah and Jameson have recently performed a detailed gradient comparison study of the *continuous* and *discrete* adjoint approaches using the Navier-Stokes equations [22], and found that in typical shape optimization problems in transonic flow the differences are small enough that they have no significant effect on the final result. The work in our group has mainly been based

on the *continuous* adjoint method. In fact this method has been successfully used for the aerodynamic design of complete aircraft configurations [8,23] and has been extended to treat aero-structural design [24].

The research in this paper addresses the validity of this design methodology for the problem of high-lift design. Traditionally, high-lift designs have been realized by careful wind tunnel testing. This approach is both expensive and challenging due to the extremely complex nature of the flow interactions that appear. CFD analyses have recently been incorporated to the high-lift design process [25,26,27]. Eyi, Lee, Rogers and Kwak have performed design optimizations of a high-lift system configuration using a chimera overlaid grid system and the incompressible Navier-Stokes equations [28]. Besnard, Schmitz, Boscher, Garcia and Cebeci performed optimizations of high-lift systems using an Interactive Boundary Layer (IBL) approach [29]. All of these earlier works on multi-element airfoil design obtained the necessary gradients by finite-difference methods. More recently discrete adjoint gradients have also been used for the design of multi-element airfoil configurations [30,31,32].

In this work, the continuous viscous adjoint method is applied to two-dimensional high-lift system designs, removing the limitations on the dimensionality of the design space by making use of the viscous adjoint design methodology. The motivation for our study of high-lift system design is twofold. On the one hand, we would like to improve the take-off and landing performance of existing high-lift systems using an adjoint formulation, while on the other hand, we would like to setup numerical optimization procedures that can be useful to the aerodynamicist in the rapid design and development of high-lift system configurations. In addition to difficulties involved in the prediction of complex flow physics, multi-element airfoils provide an additional challenge to the adjoint method: the effect of the changes in the shape of one element must be felt by the other elements in the system. While preliminary studies of the adjoint method in such a situation have already been carried out [19,33,34], this research is designed to validate the adjoint method for complex

applications of this type. Emphasis is placed on the validation and not on the creation of realistic designs, which is beyond the scope of this work.

1 Procedure

In this section we outline the overall design procedure used for a variety of design calculations that will be presented later. After the initial flowchart, each of the elements of the procedure is explained in more detail. In practical implementations of the adjoint method, a design code can be modularized into several components such as the flow solver, adjoint solver, geometry and mesh modification algorithms, and the optimization algorithm. After parameterizing the configuration of interest using a set of design variables and defining a suitable cost function, which is typically based on aerodynamic performance, the design procedure can be described as follows. First we solve the flow equations for the flow variables, followed by a solution of the adjoint equations for the costate variables subject to appropriate boundary conditions which will depend on the form of the cost function. Next we evaluate the gradients and update the aerodynamic shape based on the direction of steepest descent. Finally we repeat the process to attain an optimum configuration. A summary of the design process and a comparison with the finite-difference method are illustrated in Figure 1.

1.1 Continuous Adjoint Method

The progress of a design procedure is measured in terms of a cost function I, which could be, for example, the drag coefficient or the lift to drag ratio. For the flow about an airfoil or wing, the aerodynamic properties which define the cost function are functions of both the flow-field variables (w) and the physical location of the boundary, which may be represented by the function $\mathcal{F}$. Then

$$I = I\left(w, \mathcal{F}\right),$$

and a change in $\mathcal{F}$ results in a change

$$\delta I = \left[\frac{\partial I^T}{\partial w}\right]_I \delta w + \left[\frac{\partial I^T}{\partial \mathcal{F}}\right]_{II} \delta \mathcal{F}, \tag{1}$$

in the cost function. Here, the subscripts I and II are used to distinguish the contributions due to the variation δw in the flow solution from the change associated directly with the modification $\delta \mathcal{F}$ in the shape.

Using control theory, the governing equations of the flow field are introduced as a constraint in such a way that the final expression for the gradient does not require multiple flow solutions. This corresponds to eliminating δw from (1).

Suppose that the governing equation R which expresses the dependence of w and $\mathcal{F}$ within the flow field domain D can be written as

$$R\left(w, \mathcal{F}\right) = 0. \tag{2}$$

Then δw is determined from the equation

$$\delta R = \left[\frac{\partial R}{\partial w}\right]_I \delta w + \left[\frac{\partial R}{\partial \mathcal{F}}\right]_{II} \delta \mathcal{F} = 0. \tag{3}$$

Next, introducing a Lagrange Multiplier ψ, we have

$$\begin{aligned}
\delta I = & \left[\frac{\partial I^T}{\partial w}\right]_I \delta w + \left[\frac{\partial I^T}{\partial \mathcal{F}}\right]_{II} \delta \mathcal{F} \\
-\psi^T & \left(\left[\frac{\partial R}{\partial w}\right]_I \delta w + \left[\frac{\partial R}{\partial \mathcal{F}}\right]_{II} \delta \mathcal{F} \right) \\
& = \left\{ \frac{\partial I^T}{\partial w} - \psi^T \left[\frac{\partial R}{\partial w}\right] \right\}_I \delta w \\
& + \left\{ \frac{\partial I^T}{\partial \mathcal{F}} - \psi^T \left[\frac{\partial R}{\partial \mathcal{F}}\right] \right\}_{II} \delta \mathcal{F}.
\end{aligned}$$

Choosing ψ to satisfy the adjoint equation

$$\left[\frac{\partial R}{\partial w}\right]^T \psi = \frac{\partial I}{\partial w} \tag{4}$$

the first term is eliminated, and we find that

$$\delta I = \mathcal{G} \delta \mathcal{F}, \tag{5}$$

where

$$\mathcal{G} = \frac{\partial I^T}{\partial \mathcal{F}} - \psi^T \left[\frac{\partial R}{\partial \mathcal{F}} \right]. \tag{6}$$

The advantage is that (5) is independent of δw, with the result that the gradient of I with respect to an arbitrary number of design variables can be determined without the need for additional flow-field evaluations. In the case that (2) is a partial differential equation, the adjoint equation (4) is also a partial differential equation and the determination of the appropriate boundary conditions requires careful mathematical treatment.

The formulation of the viscous adjoint equation and the boundary conditions are described in greater detail in previous publications [35] and a detailed gradient accuracy study for the continuous adjoint method has been carried out under the assumption that both the viscosity (laminar plus turbulent) and heat conduction coefficients are essentially independent of the flow, and that their variations may be neglected [21]. This simplification has been successfully used for many aerodynamic problems of interest. However, if the flow variations result in significant changes in the turbulent eddy viscosity, it may be necessary to account for this effect in the calculation. [36,37,38].

1.2 Baseline Configuration

Wind tunnel measurements have been performed on several three-element airfoil configurations at the NASA Langley Low Turbulence Pressure Tunnel (LTPT) at various Reynolds and Mach numbers [39,40,41,42] and the results of many CFD computations for this geometry have been reported using a variety of numerical schemes for the discretization of the Navier-Stokes equations and different turbulence models [26,43,44,45]. The three-element configuration used in these studies, denoted as 30P30N, is the starting point for the present design optimization process. It must be noted that the 30P30N configuration had already been highly optimized for $C_{l_{max}}$. The relative element positioning of the slat, main element and flap are described by the rigging quantities. These variables include flap and slat deflection angles, gaps, and overlaps. The meaning of these variables can be

easily seen in Figure 2. The initial deflections of both the slat and the flap are set at 30°, the flap gap and overlap are $0.0127c/0.0025c$ whereas for the slat the gap and overlap are $0.0295c/0.025c$. In these measurements, c is the airfoil chord with the slat and flap retracted.

1.3 Grid Topology

Multi-block viscous and inviscid meshes were generated using either a C- (viscous) or O-topology (inviscid) prior to the beginning of the iterative design loop so that the flow and adjoint equations could be suitably discretized. Figure 3 shows a typical viscous multi-block mesh generated around the 30P30N configuration.

One-to-one point connectivity between block faces is employed to ensure conservation across boundaries and to provide for continuity of the grid at block interfaces. Spacing at the wall is set to be less than $2 \times 10^{-6}c$ in order to obtain $y^+ \approx 1$ based on turbulent flat plate boundary layer thickness estimates at the Reynolds number in question ($Re = 9 \times 10^6$). The use of a grid with adequately tight wall spacing ($y^+ = O(1)$) has been reported to be necessary in order to obtain accurate resolution of the wall boundary layers, wakes, and shear layers present in the problem [44,45]. Grid lines are also bunched along the expected wake trajectories of each of the elements. Once the initial grid is generated, new grids corresponding to modified airfoil shapes are obtained automatically during the design process by using a two-dimensional version of the automatic mesh perturbation scheme (WARP-MB) [10,11,23,46] that is essentially equivalent to shifting grid points along coordinate lines depending on the modifications to the shape of the boundary.

Mesh perturbations are applied only to those blocks that contain a face that is part of the 30P30N baseline configuration surface. Since the block interfaces are modified only by the motion of their end points, the initial one-to-one point connectivity between block faces remains valid throughout the complete range of surface deformations. The authors have previously handled the complexity of multi-block mesh perturbation after large baseline geometry changes [47].

1.4 Multi-block Flow and Adjoint Solvers

The prediction of high-lift flows poses a particularly difficult challenge for both CFD and turbulence modeling. Even in two-dimensions, the physics involved in the flow around a geometrically-complex high-lift device are quite sophisticated. In this study FLO103-MB, a multi-block RANS solver derived from the work of Martinelli and Jameson [48] and similar to the three-dimensional version of Reuther and Alonso [9], is used for multi-element airfoil flow-field predictions. FLO103-MB satisfies the requirements of accuracy, convergence, and robustness that are necessary in this work. FLO103-MB solves the steady two-dimensional RANS equations using a modified explicit multistage Runge-Kutta time-stepping scheme. A finite volume technique and second-order central differencing in space are applied to the integral form of the Navier-Stokes equations. The Jameson-Schmidt-Turkel(JST) scheme with adaptive coefficients for artificial dissipation is used to prevent odd-even oscillations and to allow for the clean capture of shock waves and contact discontinuities. In addition, local time stepping, implicit residual smoothing, and the multigrid method are applied to accelerate convergence to steady-state solutions. The Baldwin-Lomax algebraic model and the Spalart-Allmaras one-equation model are used to account for the Reynolds stresses. The adjoint gradient accuracy study which was presented in a previous publication [21] was based on the Baldwin-Lomax model. This model is also used for the single-element design cases in this paper. Although this algebraic model has some advantages due to its implementational simplicity and robustness, the use of this model must be restricted to design at lower angles of attack and to the design of simpler geometries such as single-element airfoils. For actual high-lift designs such as $C_{l_{max}}$ maximization, the one-equation Spalart-Allmaras model gives better predictions of both the $C_{l_{max}}$ and the flow physics around complex geometries [26,43,49].

The solution of the Spalart-Allmaras turbulence model is an adaptation of Dr. Creigh McNeil's implementation embedded in the three-dimensional version of our flow solver [50]. The trip terms are not included in the turbulence model and fully-turbulent flow is assumed. The turbu-

lence equation is solved separately from the flow equations using an alternating direction implicit (ADI) method and it is updated at the start of each multistage Runge-Kutta time step on the finest grid of the multigrid cycle only. The adjoint solution is obtained with the exact same numerical techniques used for the laminar flow solution with the assumption of *frozen* eddy viscosity. The implementation exactly mirrors the flow solution modules inside FLO103-MB, except for the boundary conditions which are imposed on the co-state variables. The parallel implementation uses a domain decomposition approach, a SPMD (Single Program Multiple Data) program structure, and the MPI standard for message passing.

1.5 Design Variables

For the present study, gaps and overlaps are used in an indirect way since the rigging is controlled by the translation of the slat and flap leading edges in the x and y directions. In this way, the element positioning variables can be more easily changed independently of each other. The actual values of overlaps and gaps can be easily recovered from the leading and trailing-edge locations of the various elements in the airfoil. The shapes of each of the elements are also used as design variables so as not to rule out the possibility that the optimum solution may be obtained with a combination of shape and position modifications. In fact, for the drag minimization of a single-element RAE2822 airfoil in transonic flow, the strong shock which appears at transonic flow conditions can only be eliminated using a small change in the shape of the airfoil. The coordinates of mesh nodes on the surface of the airfoil, Hick-Henne "*bump*" functions, patched polynomials and frequency-based decompositions can be used to represent each of the elements in the high-lift system. For example, a number of the following Hicks-Henne functions, which have been implemented and used for this study, may be added to the baseline airfoil to modify the shape:

$$b\left(x\right) = A\left[\sin\left(\pi x^{\frac{\log 5}{\log t_1}}\right)\right]^{t_2}, \qquad 0 \leq x \leq 1. \tag{7}$$

Here, A is the maximum bump magnitude, t_1 locates the maximum of the bump at $x = t_1$,

and t_2 controls the width of the bump. Using this parameterization, two options are available for obtaining the optimum $C_{l_{max}}$. Firstly, $C_{l_{max}}$ can be predicted by maximizing C_l at a given angle of attack, then predicting $C_{l_{max}}$ along a C_l vs. α line for that configuration, and repeating this procedure iteratively. In this way, the angle of attack, α, is only considered as a design variable once the intermediate shape of the airfoil has been frozen within each design cycle. Alternatively, $C_{l_{max}}$ may also be maximized directly by including angle of attack as a design variable in the optimization process.

1.6 Numerical Optimization Method

The search procedure used in this work is a simple steepest descent method in which small steps are taken in the negative gradient direction:

$$\delta \mathcal{F} = -\lambda \mathcal{G},$$

where λ is positive and small enough that the first variation is an accurate estimate of δI. Then

$$\delta I = -\lambda \mathcal{G}^T \mathcal{G} < 0.$$

After making such a modification, the gradient can be recalculated and the process repeated to follow a path of steepest descent until a minimum is reached. In order to avoid violating constraints, such as a minimum acceptable airfoil thickness, the gradient may be projected into an allowable subspace within which the constraints are satisfied. In this way, procedures can be devised which must necessarily converge at least to a local minimum.

2 Results

2.1 Validation of the Adjoint Method for Viscous Flows

This section presents the results of a gradient accuracy study for the RANS equations using the Baldwin-Lomax turbulence model as well as a simple example of the use of the resulting gradient

information in a single-element airfoil inverse design case. Gradient accuracy is assessed by comparison with finite-difference gradients and by examination of the changes in the magnitude of the gradients for different levels of flow solver convergence. For inverse design, the aerodynamic cost function chosen is given by:

$$I = \frac{1}{2} \int_{\mathcal{B}} (p - p_d)^2 \, dS, \tag{8}$$

which is simply the Euclidean norm of the difference between the current pressure distribution and a desired target, p_d, at a constant angle of attack, α. The gradient of the above cost function is obtained with respect to variations in 50 Hicks-Henne sine "bump" functions centered at various locations along the upper and lower surfaces of a baseline airfoil. The locations of these geometry perturbations are numbered sequentially such that they start at the lower surface of the trailing edge, proceed forward to the leading edge, and then back around to the upper surface of the trailing edge. Figure 4 shows a comparison between the most accurate gradients obtained using both the adjoint and finite-difference methods. There is a general agreement on all trends that validates the implementation of the present adjoint method. Some discrepancies exist which are attributed to several sources. First, there is the issue that the finite-difference gradients never achieved step size independence, and, therefore, a step size had to be selected for this plot which may not be the correct one. Second, there is the issue of mesh resolution [21]. Third, the present adjoint equation is obtained without taking into account the dependence of the dissipation coefficients on the flow variables. A detailed study on these issues was presented by Nadarajah and Jameson [22]. The source of the discrepancies is believed to be a combination of these influences.

Figure 5 shows the computed adjoint gradients for different levels of flow solver convergence. For Navier-Stokes calculations, the adjoint information is essentially unchanged if the level of convergence in the flow solver is at least 4 orders of magnitude. This is an additional advantage of using the adjoint method over finite-differencing especially for the design of high-lift configurations for which it is difficult to obtain levels of convergence much higher than 4 orders of magnitude. For

viscous flows and finite-differencing it is typical to require that the flow solver converge to about 6 orders of magnitude so that the gradient information is sufficiently accurate.

An inverse design problem which starts with an RAE2822 airfoil geometry and tries to obtain the shape that generates the pressure distribution around a NACA 64A410 airfoil at the same flow conditions is presented next. The mesh used is a Navier-Stokes C-mesh with 512×64 cells. The target pressure specified is that of the NACA 64A410 airfoil at $M_\infty = 0.75$ and $\alpha = 0°$. The Reynolds number of this calculation was set at $Re = 6.5 \times 10^6$. Figure 6 shows the progress of the inverse design calculation. In 100 design iterations, the target pressure was matched almost exactly, including the correct strength and position of the shock. The areas around the trailing-edge are very sensitive to small changes in the geometry. The source of the C_p discrepancy in the neighborhood of the trailing edge can be found in the inability of our parameterization to exactly recover the shape of the NACA 64A010 airfoil. More geometry control may be required to produce more exactly matched solutions in the areas around the trailing-edge surface. Following our design process, the initial RAE2822 airfoil geometry was altered to obtain a shape that is quite close to the NACA 64A410 airfoil that had produced the target pressure distribution in the first place. Convergence of the design procedure is simply measured by the closeness of the resulting pressure distribution to the specified target. No attempt to satisfy the Kuhn-Tucker conditions was made. The norm of the pressure error decreased over two orders of magnitude from 0.0504 to 0.0043 in 100 design iterations.

2.2 FLO103-MB with SA Model

Before using FLO103-MB with the Spalart-Allmaras (SA) turbulence model for the design of multi-element airfoils we must demonstrate that the model has been correctly implemented confirming that the solver can accurately predict the flow phenomena involved in this type of problem. In particular it is of primary importance to be able to predict the values of $C_{l_{max}}$, the element pressure

distributions, the lift curve slopes for each element and the details of the shear layers present in the problem.

Flow convergence

Figure 7 shows the convergence history of the averaged density residual for the calculation of the flow field around the 30P30N high-lift configuration using the flow solver, FLO103-MB. The Spalart-Allmaras one-equation turbulence model is used for this calculation. The solution converges down to somewhere in the range of 10^{-4} and 10^{-5} in about 2000 iterations. Although small oscillations in the residual remain after 2000 iterations, the C_l, one of the cost functions used for subsequent designs, has converged without oscillations. As mentioned earlier, this level of convergence is also sufficient to obtain accurate sensitivity information using the adjoint method.

Comparisons with Experimental Data

Comparisons between computational results and experimental data are presented below for validation purposes. The code, FLO103-MB, and the related turbomachinery code TFLO [51], have been extensively validated for a variety of test cases, ranging from flat plates and transonic axisymmetric bumps, to full three-dimensional configurations.

Figure 8, shows the comparison of the computational and experimental C_p distributions around the 30P30N configuration at $M_\infty = 0.2$, $\alpha = 8^\circ$, and Re$= 9 \times 10^6$. The agreement between experimental and computational distributions is very encouraging. Integrated force coefficients also agree quite well.

In order to validate the ability of the flow solver to predict stall using the SA turbulence model, a comparison of C_l versus angle of attack is shown in Figure 9. The total coefficient of lift, together with the individual lift from the three components, is plotted in the range of $-5^\circ < \alpha < 25^\circ$. The computed results agree quite well with experiment with slightly higher predictions of $C_{l_{max}}$ and

angle of attack at $C_{l_{max}}$. Although the results do not agree with the experiment exactly, it has been observed that the choice of turbulence model can have a substantial impact on the numerical values of some of these parameters. The stall prediction capability can be a critical factor for actual design cases, such as $C_{l_{max}}$ maximization. With other turbulence models, these quantities can be over-predicted substantially.

2.3 Single-Element Airfoil Design

Before embarking on multi-element airfoil design, a study of the use of optimization for single-element airfoils was performed to gain insight into the possibilities for improvements and the behavior of the method. C_d minimization at a fixed C_l and C_l maximization at a fixed C_d were tested in order to guarantee the improvement of the lift over drag ratio, L/D, which is a measure of the aerodynamic efficiency. The design examples presented in this subsection were all carried out using a 4 block multi-block mesh around an RAE2822 airfoil with a total number of cells equal to 512×64. The two designs presented had as a starting point the RAE2822 airfoil and computations were carried out at a Reynolds number of 6.5 million. The surface of the airfoil was parameterized using 50 Hicks-Henne bump functions, 25 of which are distributed evenly along the upper surface of the airfoil, while the remaining 25 are placed in a similar fashion along the lower surface.

C_d Minimization at a Fixed C_l

Figure 10 shows the result of a typical viscous design calculation where the total coefficient of drag of the airfoil is minimized using the parameterization described above. The free stream Mach number is 0.73 and the optimization procedure is forced to achieve a near constant $C_l = 0.83$. This constraint is achieved by periodically adjusting the angle of attack during the flow solution portion of the design procedure in what is sometimes called a *reduced* gradient approach. Figure 10 shows the result of 50 design iterations for this test case. The optimizer is able to eliminate the strong

shock wave that existed in the initial design by using the values of the same 50 design variables. Once the design process is completed, the total coefficient of drag has been reduced from 0.0167 to 0.0109, while the C_l has increased very slightly from 0.8243 to 0.8305. The L/D has improved by 54.36% from 49.36 to 76.19. This test case also provides a validation of the multi-block design procedure, since a similar test case had previously been run using the single-block design code.

C_l Maximization at a Fixed C_d

In this test case, we attempt to maximize the C_l of the RAE2822 airfoil by altering its shape using the same 50 Hicks-Henne design functions while constraining the coefficient of drag to be constant ($C_d = 0.0153$). Figure 11 shows the result of this type of design optimization. The front portion of the upper surface of the configuration is modified considerably to produce a very different pressure distribution that allows for the existence of a shock wave on the upper surface that considerably increases the amount of lift carried by the airfoil. In addition, since the C_d is constrained to be constant (this is imposed by allowing the angle of attack to float), the resulting angle of attack is also higher, again leading to the creation of a higher lift coefficient. The numerical results presented show significant improvements in L/D. The resulting L/D increased 21.70% from 52.22 to 63.55.

2.4 Multi-Element Airfoil Design

Except for the inviscid test case presented in the first subsection below, all of the results in this section were computed using multi-block viscous meshes constructed using a C-topology. The C-topology mesh has 26 blocks of varying sizes and a total of 204,800 cells. All calculations were carried out at a free stream Mach number, $M_\infty = 0.20$ and a Reynolds number, Re$= 9 \times 10^6$. The computation of the Reynolds stress was carried out using the Spalart-Allmaras turbulence model. Apart from the first inviscid test case, the results in this section mimic those in the single-element airfoil section.

Inverse Design Using the Euler Equations

In order to verify the implementation of our design procedure, we present a simple test case which is aimed at verifying that the multi-block flow and adjoint solvers are capable of producing correct sensitivities to both shape modifications and rigging variables in a multi-element airfoil design environment. For this purpose, a multi-block inviscid grid around the 30P30N configuration was constructed. A perturbed geometry was created by activating a single bump on the upper surface of the main element and by deflecting the flap by an increment of 2°. The pressure distribution around the original geometry is used as a target pressure distribution (seen as a solid line in Figure 12) for the perturbed geometry to arrive at through an inverse design process. Because this target pressure distribution is achievable, we can indirectly measure the correctness of the sensitivity information by observing whether the design evolves towards the known specified target. Notice that the modification of the geometry described above influences the pressure distribution in all three elements: slat, main element, and flap.

A total of 156 design variables were used to parameterize the complete configuration, including 50 bump functions in each of the three elements. In addition, both the slat and the flap were allowed to translate in the x and y directions and to rotate about their leading-edges. After 100 design iterations where sensitivities with respect to all design variables were calculated, the target pressure distribution was recovered as expected. The original geometry was also recovered as shown in Figure 12. Figure 13 shows the convergence history of the objective function. The results of this inviscid test case provide the necessary confidence to tackle some of the more complex viscous cases presented below.

C_d Minimization at a Fixed C_l

In this test case, we attempt to minimize the total drag coefficient of the configuration without changing the lift coefficient. This design task is one of the most interesting problems since decreasing

C_d without loss in C_l is the most effective way of increasing the lift over drag ratio of airfoil at low Mach number (no shock waves) and at high angle of attack flight conditions (high initial lift coefficient). However, this case is also the most difficult one, since a decrease in C_d usually comes at the expense of a decrease in C_l for the high-lift system configuration design. Notice that, as opposed to the single-element test case, the Mach number of the flow is subsonic throughout ($C_{p_{crt}} = -16.3$ for $M_\infty = 0.2$) and, therefore, no shock waves are present. A total of 9 design iterations were carried out and, as expected, with a slight increase in C_l, a small decrease (10 drag counts) in C_d was achieved as shown in Figure 14. The resulting L/D increases by 1.73% from 62.17 (Baseline L/D at $\alpha = 16.02°$) to 63.25. Notice that the resulting α has increased slightly while trying to maintain C_l unchanged.

C_l Maximization at a Fixed Angle of Attack

We now maximize the C_l of the configuration using all 156 design variables in the problem. In this test case, the angle of attack of the whole configuration remains constant, $\alpha = 16.02°$. The optimizer is able to make improvements in C_l after 19 design iterations: the lift coefficient has increased from 4.0412 to 4.1881 as shown in Figure 15. Large changes are observed in both the flap and slat deflection angles. The flap deflection angle has increased from 30°to 32.6° in order to allow for larger camber and the slat deflection angle has decreased from 30°to 26.7° achieving a higher effective angle of attack, and therefore carrying more lift. Changes in gaps and overlaps are small and the resulting flap gap and overlap are $0.0153c/0.0020c$ whereas for the slat the gap and overlap are $0.0309c/0.0258c$. Figure 16 shows the same design attempt using only the setting parameters as the design variables. After 19 design iterations, the lift coefficient has increased from 4.0412 to 4.1698. From these results it is evident that a large portion (about 85%) of the increase in C_l is due to the modification of the rigging parameters of each airfoil element. However, notice that very small geometry changes in each element through the bump functions still delivered more

than 100 counts (15% of the increase) in lift coefficient.

C_l Maximization at a Fixed C_d

We now allow the angle of attack of the configuration to float by fixing the value of C_d to that of the baseline design point at $\alpha = 16.02°$. As we can see in Figure 17, in 10 design iterations, the optimizer has increased the lift by 815 counts from 4.0412 to 4.1227 while reducing the angle of attack from 16.02° to 15.127° with small changes in the total coefficient of drag from 0.0650 to 0.0661. This result appears counterintuitive at first but highlights the power of both the adjoint methodology and the careful parameterization of the surface, since the procedure still yields a higher C_l, while the angle of attack is forced down to match the prescribed $C_d = 0.0650$.

2.5 Maximum Lift Maximization

2.5.1 Single-Element Airfoil Results

The present adjoint method was also applied to the optimization of an airfoil shape that maximizes the maximum lift coefficient ($C_{l_{max}}$). The RAE2822 single-element airfoil and the same 4 block mesh used for the previous single-element airfoil design cases were used for calculations at a design condition of $M_\infty = 0.2$ and $Re = 6.5 \times 10^6$. Bump functions were used as before, and the angle of attack (α) was included as an additional design variable for the maximization of maximum lift. Two different approaches were tried. In the first approach three steps were taken as follows: firstly using α alone as a design variable, $C_{l_{max}}$ and α at $C_{l_{max}}(\alpha_{clmax})$ were predicted along the C_l vs. α curve for the baseline configuration and then, using 50 bump functions, a new airfoil configuration was obtained that maximized C_l with $\alpha = \alpha_{clmax}$ fixed. Finally, starting from this value of α, the first step was repeated to obtain a new $C_{l_{max}}$ and new α_{clmax} for the updated configuration. Figure 18 shows the design results from this approach. In the first step, $C_{l_{max}}$ was predicted to be 1.6430 at $\alpha_{clmax} = 14.633°$ (O – A in Figure 20). Next, as shown in Figure 19, $C_{l_{max}}$ increased

to 1.8270 while the initial airfoil was updated to have more thickness near the leading-edge and more camber (A – B in Figure 20). The final $C_{l_{max}}$ obtained was 1.8732 (Point C in Figure 20) and the overall $C_{l_{max}}$ improved 14% from 1.6430 while α_{clmax} increased 11.1% from 14.633° to 16.250°. This design example verifies the design capabilities of the adjoint gradients using α. Although this example represents a single iteration of the overall procedure (note that 31 iterations were used during the A – B step), this procedure could be repeated iteratively to attain even higher levels of $C_{l_{max}}$.

Based on the information gathered from the first approach, both the bumps and the angle of attack were simultaneously used for the design in the second approach (D – E in Figure 20). As shown in Figure 21, using the baseline RAE2822 at $\alpha = 11.85°$, $C_{l_{max}}$ improved by 13.3% to 1.8617 and α_{clmax} changed by 6.8% to 15.623° from the $C_{l_{max}}$ and α_{clmax} of the baseline RAE2822 configuration.

2.5.2 Multi-Element Airfoil Results

This design example is the culmination of the efforts in this paper. Using the newly developed viscous adjoint procedure, the multi-block flow and adjoint solvers, and the lessons learned in the previous design examples, we can now attempt to redesign the $30P30N$ multi-element airfoil to optimize its value of $C_{l_{max}}$. In this case, a total of 157 design variables are used, including 50 Hicks-Henne bump functions on each of the three elements, 3 rigging variables for each the slat and flap components, and the angle of attack (α) of the complete configuration.

As shown in Figure 22, the design started at $\alpha = 22°$ which is near the α_{clmax} of the baseline $30P30N$ configuration and the baseline was modified in the direction of C_l improvement using all of the design variables. As shown in Figure 22 and Figure 23, $C_{l_{max}}$ improved by 1.12%, 501 counts, increasing from 4.4596 to 4.5097, with a slight change (0.43%) in α_{clmax}. Even for highly optimized configuration such as the 30P30N, further small improvements can be achieved by using the viscous

adjoint sensitivities that are the central portion of this paper.

2.6 Results of Design Optimization

In the present design study all of the optimizations employed the method of steepest descent. Constraints are applied in the optimization by simply projecting the gradient vector onto the subspace of feasible designs, eventually leading to a constrained optimum which is arrived at by moving along constraint boundaries. No attempt to use an augmented Lagrangian was made and therefore, the actual optimum design is not measured by the satisfaction of the Kuhn-Tucker conditions, but, instead, by monitoring the progress of the cost function of interest. Obviously, a non-linear constrained optimizer could have been used instead (as we have done in some of our previous work [10,11].) However, we have often found that, in engineering terms, solutions very close to the optimum can be found with the steepest descent method. Although for gradient-based optimization, convergence to the exact optimum cannot be expected in fewer iterations than the actual number of design variables in the problem, in typical adjoint-based design parameterizations, it is not unusual to have design variables whose gradients are rather small and, therefore, have very little effect on the value of the cost function at the optimum point. For this reason, some of the design calculations were stopped after a given number of design iterations, once the function of interest showed no evidence of continued decrease.

Figure 24 shows the convergence history for the C_l maximization of the RAE2822 airfoil using the angle of attack as the only design variable. As expected by the theory, C_l converged to the local maximum and the gradient value corresponding to the local optimum became 3.096×10^{-6} of its initial value, 6.506, in 44 design iterations.

Similarly, for the problem of drag minimization of an RAE2822 airfoil at a fixed angle of attack, the local minimum for the specified parameterization was achieved as shown in Figure 25. However, this minimum may be further improved if a different shape parameterization were to be employed;

the present design parameterization did not allow for modifications of the leading and trailing edge locations and all of the Hicks-Henne "*sine bump*" functions had fixed a, t_1, and t_2 parameters (in Equation 7) and therefore, the numerical optimization procedure was unable to span the complete design space of all possible airfoil shapes. Although no direct constraints were introduced, the use of the present *bump* functions (with bounds on their possible values) and design parameterization can be considered an indirect way of applying constraints.

In the single-element lift maximization cases using Hicks-Henne bump functions, the designs were run for a pre-specified number of design iterations and were not necessarily allowed to converge to the exact local maximum, although inspection of the results reveals that the difference was small. Further improvements can be obtained by reducing the airfoil thickness and therefore, a more complete treatment of thickness constraints is suggested for more detailed design work.

For the multi-element design cases, the relative improvements were smaller than those of the single-element design cases. The lift increments, however, are of comparable magnitude although the baseline values for the multi-element cases are much higher. One of the main reasons for this was the fact that the baseline high-lift configuration was already a highly optimized one. Two other possible reasons can also be mentioned. Firstly, the additional design variables such as the flap and slat deflection angles, gaps, and overlaps, made the multi-element airfoil design space much more complex than that of the single-element airfoil design. For the scalings used in both the bump amplitudes and the flap and slat angle deflections, the magnitudes of the lift and drag sensitivities differ considerably. Typically, for the units chosen in this work, the sensitivities to the bump amplitudes are much larger then those due to angle of attack variations, although the cost function improvements that may be derived from angle of attack changes may be more substantial after a large number of steepest descent design iterations. Since, due to the cost of the optimization procedure for viscous multi-element design, we were limited in the total number of design iterations that we could compute, a user-defined scaling was used in the angle of attack variables to arrive at

the local minimum in a smaller number of iterations. Secondly, one can expect further improvements by using alternative cost functions and adjoint boundary conditions. Interestingly, for the drag minimization of the multi-element configuration, a significant improvement was observed using pressure drag as the cost function instead of total drag, though the actual numerical result was not included in this paper since a thorough study has not been completed. This may be due to the fact that most of the drag of the multi-element airfoil is the pressure drag. Although the flow in high-lift systems is dominated by viscous phenomena, the typical ratio of pressure drag to skin friction drag is of order of 10.

The high-lift system optimizations of the 30P30N configuration were carried out using a multi-block mesh with 26 blocks and a total of 204,800 mesh points. Each design iteration involved the solution of the flow using the Spalart-Allmaras turbulence model and it required about $5,000$ iterations. The adjoint solution is computed in the same mesh and, since it does not need to be converged as far as the flow solution in order to obtain accurate gradient information, only 700 iterations were required. Each design iteration, consisting of one flow and one adjoint solution and all the necessary mesh perturbations and gradient calculations took approximately 1.5 hr on 26 processors of an SGI Origin 2000 computer with the 195MHz R10000 processor.

3 Conclusions

A numerical optimization procedure using the adjoint method for high-lift system design has been developed and presented. The procedure is based on a multi-block RANS flow solver, FLO103-MB, that uses the Spalart-Allmaras turbulence model for high Reynolds number flows. FLO103-MB has been implemented in parallel so that the turnaround for design calculations can be even faster.

Multi-element airfoils are parameterized using the well-known Hicks-Henne bump functions and additional design variables that allow the gaps and overlaps, as well as the angle of attack of the slat and flap elements to be represented. Making use of the large computational savings provided by the

adjoint method when large numbers of design variables are involved, we are able to explore high-dimensional design spaces that are necessary for high-lift system design. In this study, the 30P30N multi-element airfoil is used because experimental data is available for validation purposes. A total of 157 design variables corresponding to 50 Hicks-Henne bump functions on each of the elements of the configuration, the x and y locations and angles of attack of the slat and flap elements, and the overall angle of attack of the configuration are used for C_d minimization and C_l maximization subject to several kinds of constraints. The angle of attack of the high-lift system was used as a design variable for $C_{l_{max}}$ maximization only.

Results for L/D maximization, and $C_{l_{max}}$ maximization for the RAE2822 single-element airfoil showed significant improvements. For the multi-element design cases, the relative improvements were smaller than those of the single-element design cases. The lift increments, however, are of comparable magnitude although the baseline values for the multi-element cases are much higher. Of course, one of the main reasons for this was the fact that the baseline high-lift configuration was already a highly optimized one. The results obtained are encouraging and point out that the adjoint method can have great potential for the design of high-lift systems. The design cases in this work are purely academic and meant to validate the sensitivity calculation procedure only. Future work will focus on expanding current results and on utilizing the method described above to perform realistic two-dimensional high-lift system designs.

4 Acknowledgments

This research has been made possible by the generous support of the David and Lucille Packard Foundation in the form of a Stanford University School of Engineering Terman fellowship. The authors acknowledge Dr. Creigh MaNeil for assistance with his implementation of the Spalart-Allmaras turbulence model in the three-dimensional version of our flow solver. Thanks also go to Dr. Kuo-Cheng of the Boeing Company for providing us with the multi-element airfoil experimental

data.

References

[1] F. Bauer, P. Garabedian, D. Korn, and A. Jameson. *Supercritical Wing Sections II.* Springer Verlag, New York, 1975.

[2] P. R. Garabedian and D. G. Korn. Numerical design of transonic airfoils. In B. Hubbard, editor, *Proceedings of SYNSPADE 1970*, pages 253–271, Academic Press, New York, 1971.

[3] R. M. Hicks and P. A. Henne. Wing design by numerical optimization. *Journal of Aircraft*, 15:407–412, 1978.

[4] J. Fay. *On the Design of Airfoils in Transonic Flow Using the Euler Equations.* Ph.D. Dissertation, Princeton University 1683-T, 1985.

[5] R. Campbell. An approach to constrained aerodynamic design with application to airfoils. *NASA Technical Paper 3260*, Langley Research Center, November 1992.

[6] A. Jameson. Aerodynamic design via control theory. *Journal of Scientific Computing*, 3:233–260, 1988.

[7] A. Jameson. Optimum aerodynamic design using CFD and control theory. *AIAA paper 95-1729*, AIAA 12th Computational Fluid Dynamics Conference, San Diego, CA, June 1995.

[8] J. Reuther, A. Jameson, J. Farmer, L. Martinelli, and D. Saunders. Aerodynamic shape optimization of complex aircraft configurations via an adjoint formulation. *AIAA paper 96-0094*, 34th Aerospace Sciences Meeting and Exhibit, Reno, Nevada, January 1996.

[9] J. Reuther, J. J. Alonso, J. C. Vassberg, A. Jameson, and L. Martinelli. An efficient multiblock method for aerodynamic analysis and design on distributed memory systems. *AIAA paper 97-1893*, June 1997.

[10] J. J. Reuther, A. Jameson, J. J. Alonso, M. Rimlinger, and D. Saunders. Constrained multipoint aerodynamic shape optimization using an adjoint formulation and parallel computers: Part I. *Journal of Aircraft*, 36(1):51–60, 1999.

[11] J. J. Reuther, A. Jameson, J. J. Alonso, M. Rimlinger, and D. Saunders. Constrained multipoint aerodynamic shape optimization using an adjoint formulation and parallel computers: Part II. *Journal of Aircraft*, 36(1):61–74, 1999.

[12] J. R. R. A. Martins, I. M. Kroo, and J. J. Alonso. An automated method for sensitivity analysis using complex variables. *AIAA paper 2000-0689*, 38th Aerospace Sciences Meeting, Reno, Nevada, January 2000.

[13] C. Bischof, A. Carle, G. Corliss, A. Griewank, and P. Hovland. Generating derivative codes from Fortran programs. *Internal report MCS-P263-0991*, Computer Science Division, Argonne National Laboratory and Center of Research on Parallel Computation, Rice University, 1991.

[14] J.L. Lions. *Optimal Control of Systems Governed by Partial Differential Equations*. Springer-Verlag, New York, 1971. Translated by S.K. Mitter.

[15] O. Pironneau. *Optimal Shape Design for Elliptic Systems*. Springer-Verlag, New York, 1984.

[16] A. Jameson. Re-engineering the design process through computation. *AIAA paper 97-0641*, 35th Aerospace Sciences Meeting and Exhibit, Reno, Nevada, January 1997.

[17] J. Reuther, J.J. Alonso, M.J. Rimlinger, and A. Jameson. Aerodynamic shape optimization of supersonic aircraft configurations via an adjoint formulation on parallel computers. *AIAA*

paper 96-4045, 6th AIAA/NASA/ISSMO Symposium on Multidisciplinary Analysis and Optimization, Bellevue, WA, September 1996.

[18] O. Baysal and M. E. Eleshaky. Aerodynamic design optimization using sensitivity analysis and computational fluid dynamics. *AIAA paper 91-0471*, 29th Aerospace Sciences Meeting, Reno, Nevada, January 1991.

[19] W. K. Anderson and V. Venkatakrishnan. Aerodynamic design optimization on unstructured grids with a continuous adjoint formulation. *AIAA paper 97-0643*, 35th Aerospace Sciences Meeting and Exhibit, Reno, Nevada, January 1997.

[20] A. Jameson, N. Pierce, and L. Martinelli. Optimum aerodynamic design using the Navier-Stokes equations. *AIAA paper 97-0101*, 35th Aerospace Sciences Meeting and Exhibit, Reno, Nevada, January 1997.

[21] S. Kim, J. J. Alonso, and A. Jameson. A gradient accuracy study for the adjoint-based navier-stokes design method. *AIAA paper 99-0299*, AIAA 37th Aerospace Sciences Meeting & Exhibit, Reno, NV, January 1999.

[22] S. Nadarajah and A. Jameson. Studies of the continuous and discrete adjoint approaches to viscous automatic aerodynamic shape optimization. *AIAA paper 2001-2530*, AIAA 15th Computational Fluid Dynamic Conference, Anaheim, CA, June 2001.

[23] J. Reuther, A. Jameson, J. J. Alonso, M. J. Rimlinger, and D. Saunders. Constrained multipoint aerodynamic shape optimization using an adjoint formulation and parallel computers. *AIAA paper 97-0103*, 35th Aerospace Sciences Meeting and Exhibit, Reno, Nevada, January 1997.

[24] J. R. R. A. Martines. A coupled-adjoint method or high-fidelity aero-structural optimization. *Ph. D. Dissertation*, Stanford University, 2002.

[25] S. X. Ying. High lift challenges and directions for cfd. Technical report, AIAA/NPU AFM Conference Proceedings, China, June 1996.

[26] Christopher L. Rumsey, Thomas B. Gatski, Susan X. Ying, and Arild Bertelrud. Prediction of high-lift flows using turbulent closure models. *AIAA Journal*, 36:765–774, 1998.

[27] Christopher L. Rumsey and Susan X. Ying. Prediction of high-lift: Review of present cfd capability. *Progress in Aerospace Sciences*, 38(2):145–180, 2002.

[28] S. Eyi, K. D. Lee, S. E. Rogers, and D. Kwak. High-lift design optimization using navier-stokes equations. *Journal of Aircraft*, 33:499–504, 1996.

[29] Eric Besnard, Adeline Schmitz, Erwan Boscher, Nicolas Garcia, and Tuncer Cebeci. Two-dimensional aircraft high lift system design and optimization. *AIAA paper 98-0123*, 1998.

[30] Marian Nemec and David W. Zingg. From analysis to design of high-lift configurations using a newton-krylov algorithm. *ICASE 2002 Congress*, 2002.

[31] Marian Nemec, David W. Zingg, and T.H. Pulliam. Multi-point and multi-objective aerodynamic shape optimization. *AIAA paper 2002-5548*, 2002.

[32] C. S. Kim. Sensitivity analysis for the navier-stokes equations with a two-equation turbulence models and its applications. *Ph. D. Dissertation*, Seoul National University, Seoul, Korea, 2001.

[33] S. Kim, J. J. Alonso, and A. Jameson. Two-dimensional high-lift aerodynamic optimization using the continuous adjoint method. *AIAA paper 2000-4741*, 8th AIAA/USAF/NASA/ISSMO Symposium on Multidisciplinary Analysis and Optimization, Long Beach, CA, September 2000.

[34] A. Jameson S. Nadarajah and J.J. Alonso. An adjoint method for the calculation of remote sensitivities in supersonic flow. *AIAA paper 2002-0261*, 30th AIAA Aerospace Sciences Meeting, Reno, NV, January 2002.

[35] A. Jameson, L. Martinelli, and N. A. Pierce. Optimum aerodynamic design using the Navier-Stokes equations. *Theoretical and Computational Fluid Dynamics*, 10:213–237, 1998.

[36] W. Kyle Anderson and Dary L. Bonhaus. Navier-stokes computations and experimental comparisons for multielement airfoil configurations. *AIAA Journal*, 37(2):185–191, 1999.

[37] Marian Nemec and David W. Zingg. Newton-krylov algorithm for aerodynamic design using the navier-stokes equations. Technical Report 6, 2002.

[38] C. S. Kim, C. Kim, and O. H. Rho. Effects of constant turbulent eddy viscosity assumption on gradient-based design optimization. *AIAA paper 2002-0262*, 2001.

[39] W. O. Valarezo. High lift testing at high reynolds numbers. *AIAA paper 92-3986*, AIAA 9th Aerospace Ground Testing Conference, Nashville, TN, July 1992.

[40] W. O. Valarezo, C. J. Dominik, R. J. McGhee, W. L. Goodman, and K. B. Paschal. Multi-element airfoil optimization for maximum lift at high reynolds numbers. In *Proceedings of the AIAA 9th Applied Aerodynamics Conference*, pages 969–976, Washington, DC, 1991.

[41] V. D. Chin, D. W. Peter, F. W. Spaid, and R. J. McGhee. Flowfield measurements about a multi-element airfoil at high reynolds numbers. *AIAA paper 93-3137*, July 1993.

[42] F. W. Spaid and F. T. Lynch. High reynolds numbers, multi-element airfoil flowfield measurements. *AIAA paper 96-0682*, AIAA 34th Aerospace Sciences Meeting & Exhibit, Reno, NV, Jan 1996.

[43] S. E. Rogers, F. R. Menter, and P. A. Durbin Nagi N. Mansour. A comparison of turbulence models in computing multi-element airfoil flows. *AIAA paper 94-0291*, AIAA 32nd Aerospace Sciences Meeting & Exhibit, Reno, NV, January 1994.

[44] S. E. Rogers. Progress in high-lift aerodynamic calculations. *AIAA paper 93-0194*, AIAA 31st Aerospace Sciences Meeting & Exhibit, Reno, NV, January 1993.

[45] W. Kyle Anderson and Dary L. Bonhaus. Navier-stokes computations and experimental comparisons for multielement airfoil configurations. *Journal of Aircraft*, 32:1246–1253, 1993.

[46] J. Reuther, A. Jameson, J. Farmer, L. Martinelli, and D. Saunders. Aerodynamic shape optimization of complex aircraft configurations via an adjoint formulation. *AIAA paper 96-0094*, AIAA 34th Aerospace Sciences Meeting and Exhibit, Reno, NV, January 1996.

[47] S. Kim, J. J. Alonso, and A. Jameson. Design optimization of high-lift configurations using a viscous continuous adjoint method. *AIAA paper 2002-0844*, AIAA 40th Aerospace Sciences Meeting & Exhibit, Reno, NV, January 2002.

[48] L. Martinelli and A. Jameson. Validation of a multigrid method for the Reynolds averaged equations. *AIAA paper 88-0414*, 1988.

[49] P. R. Spalart and S. R. Allmaras. A one-equation turbulence model for aerodynamic flows. *AIAA paper 92-0439*, AIAA 30nd Aerospace Sciences Meeting & Exhibit, Reno, NV, January 1992.

[50] C.Y. McNeil. Turbomachinery simulations: Spalart-allmaras turbulence model implementation. Contributed secton to center for integrated turbulence simulations annual technical report, Stanford University, 1999.

[51] J.J. Alonso J. Yao, RogerL. Davis and A. Jameson. Unsteady flow investigations in an axial turbine using massively parallel flow solver tflo. *AIAA paper 2001-0529*, 39th AIAA Aerospace Sciences Meeting, Reno, NV, January 2001.

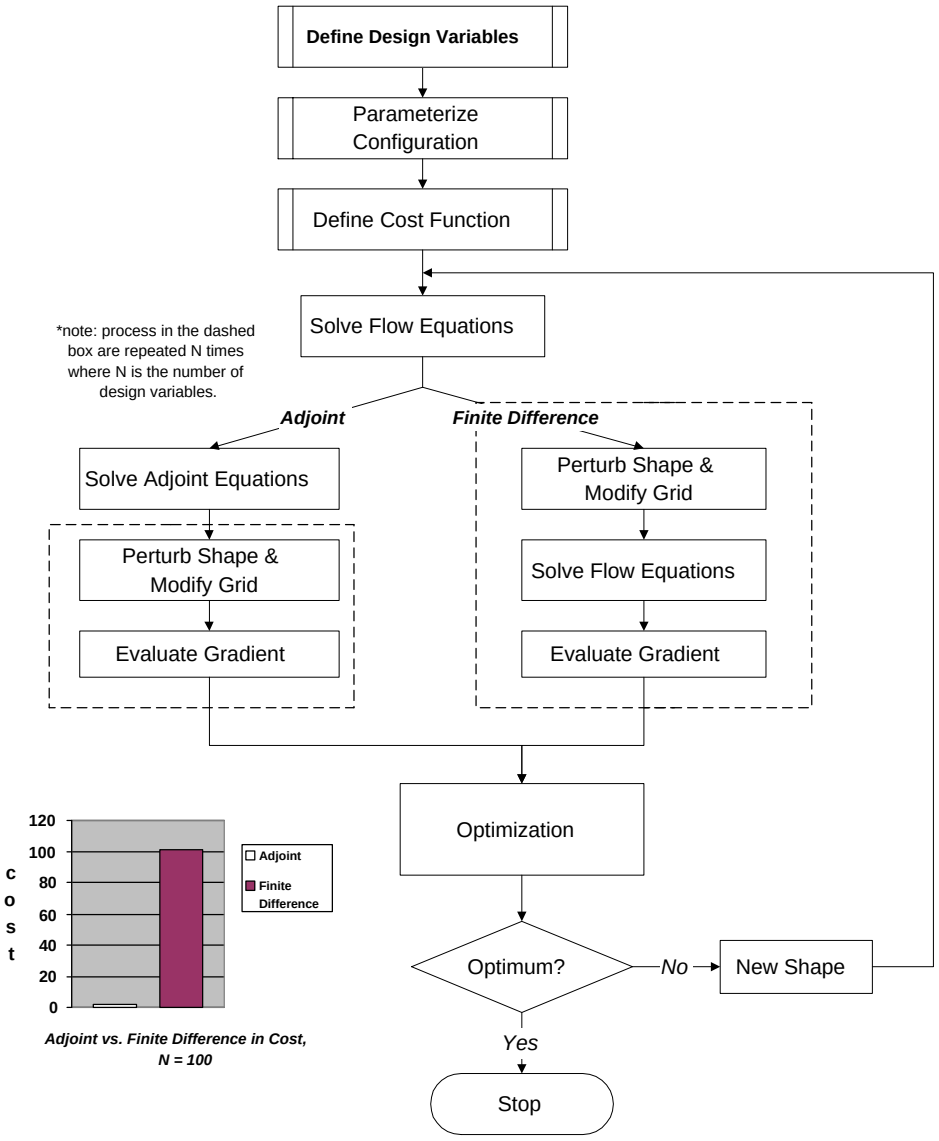

Figure 1: Flowchart of the design process.

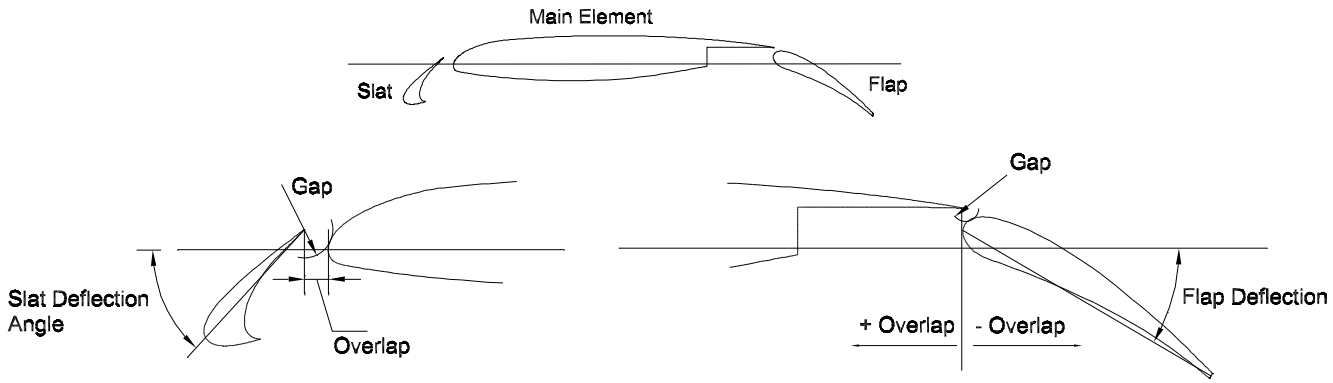

Figure 2: Definitions of gap, overlap, and deflection angles.

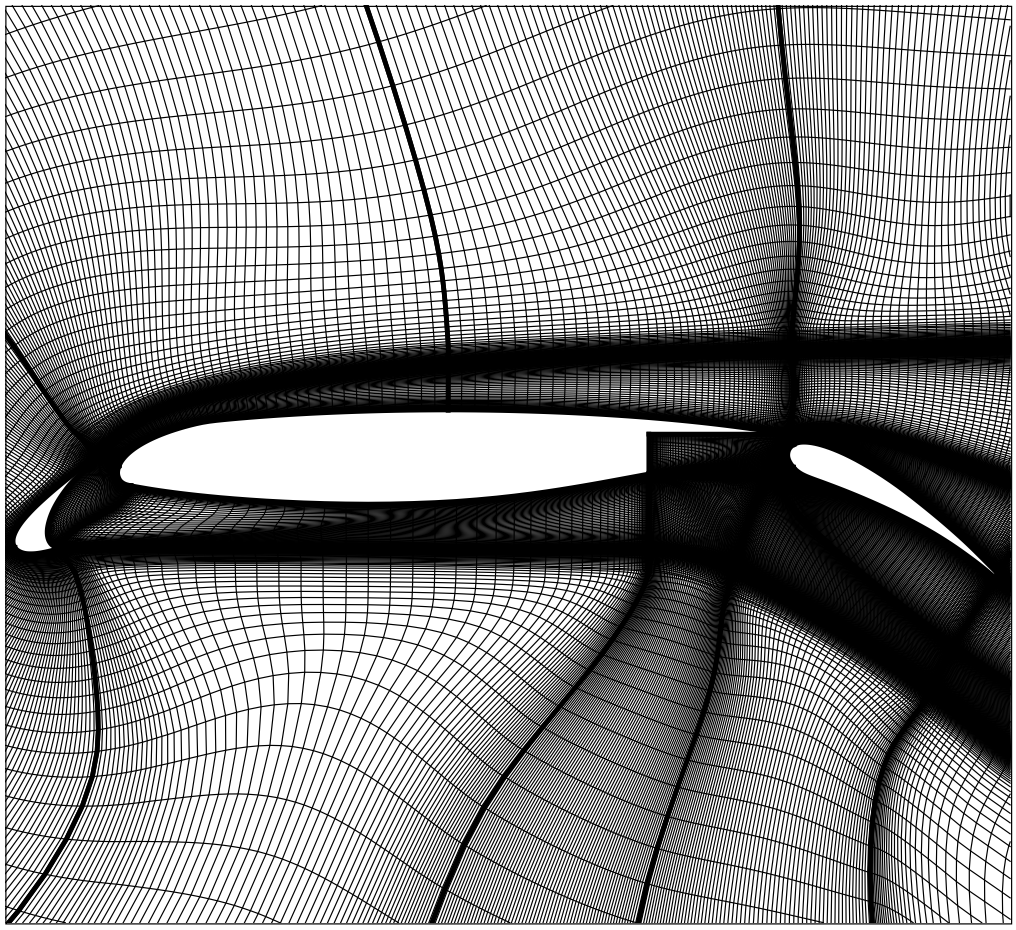

Figure 3: Grid around the 30P30N multi-element configuration.

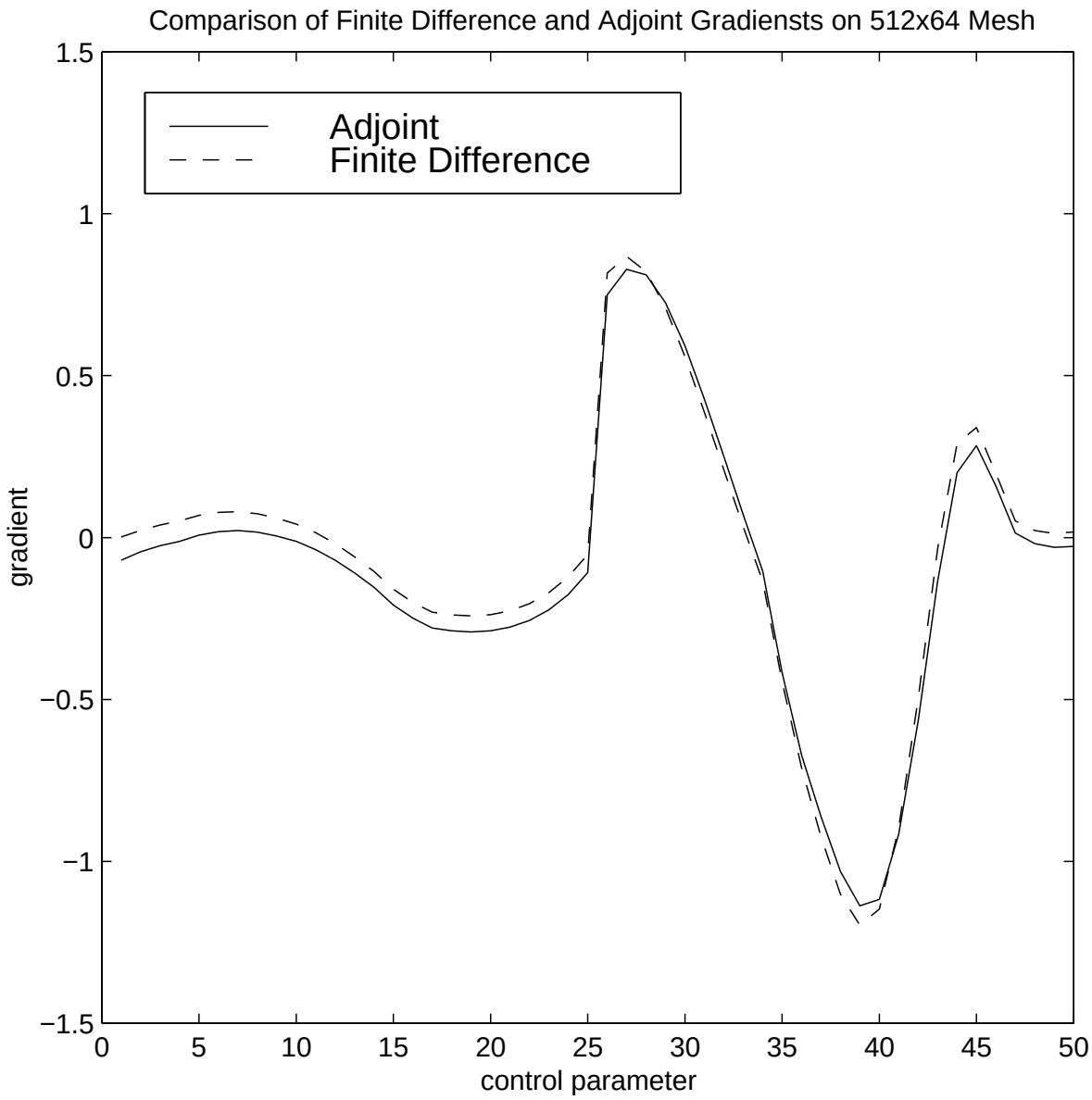

Figure 4: Navier-Stokes inverse design: comparison of finite-difference and adjoint gradients for a 512x64 mesh.

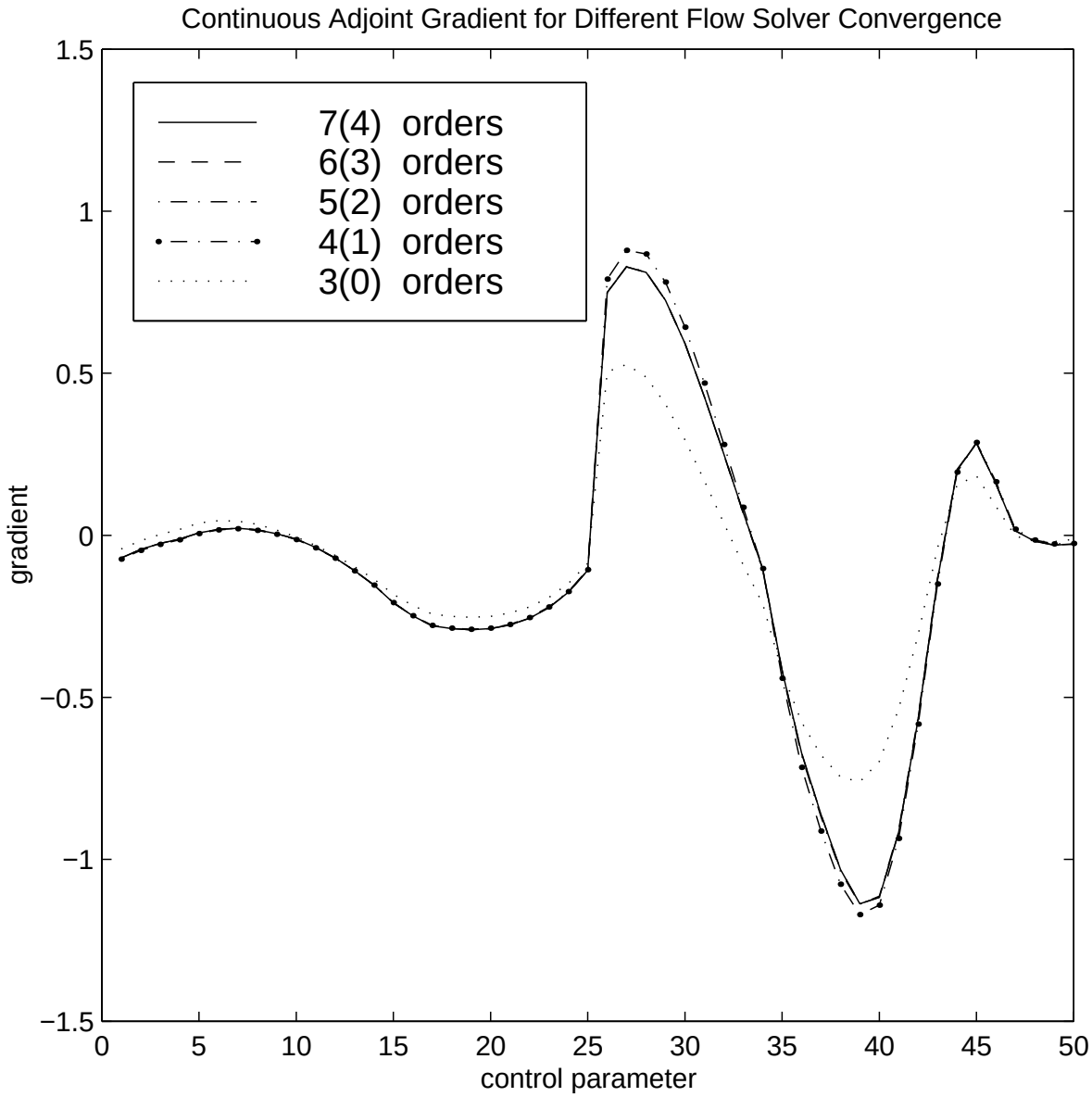

Figure 5: Navier-Stokes inverse design: adjoint gradients for varying levels of flow solver convergence.

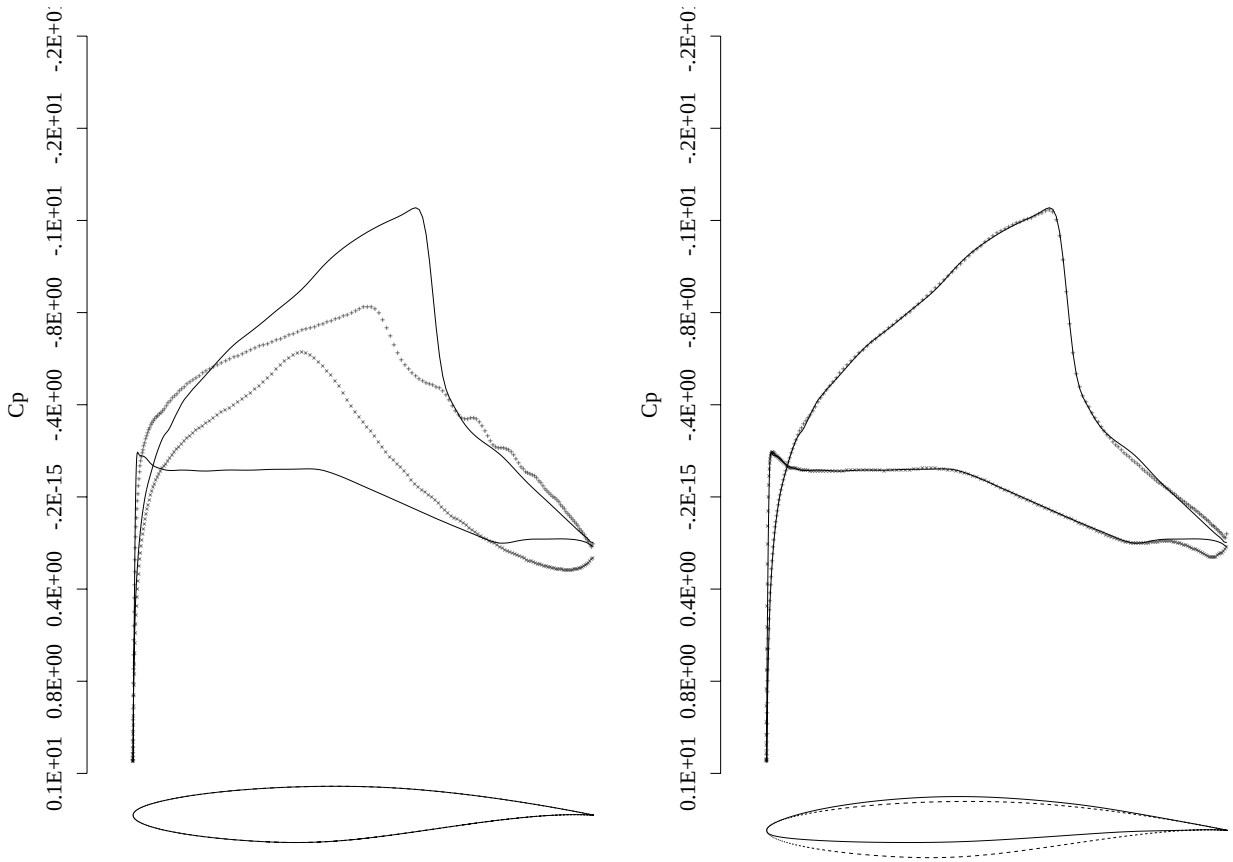

6a: Initial, $P_{error} = 0.0504$.

6b: 100 design iterations, $P_{error} = 0.0043$.

Figure 6: Typical Navier-Stokes inverse design calculation, RAE 2822 airfoil to NACA 64A410, $M_\infty = 0.75$, $\alpha = 0°$, Re $= 6.5 \times 10^6$.

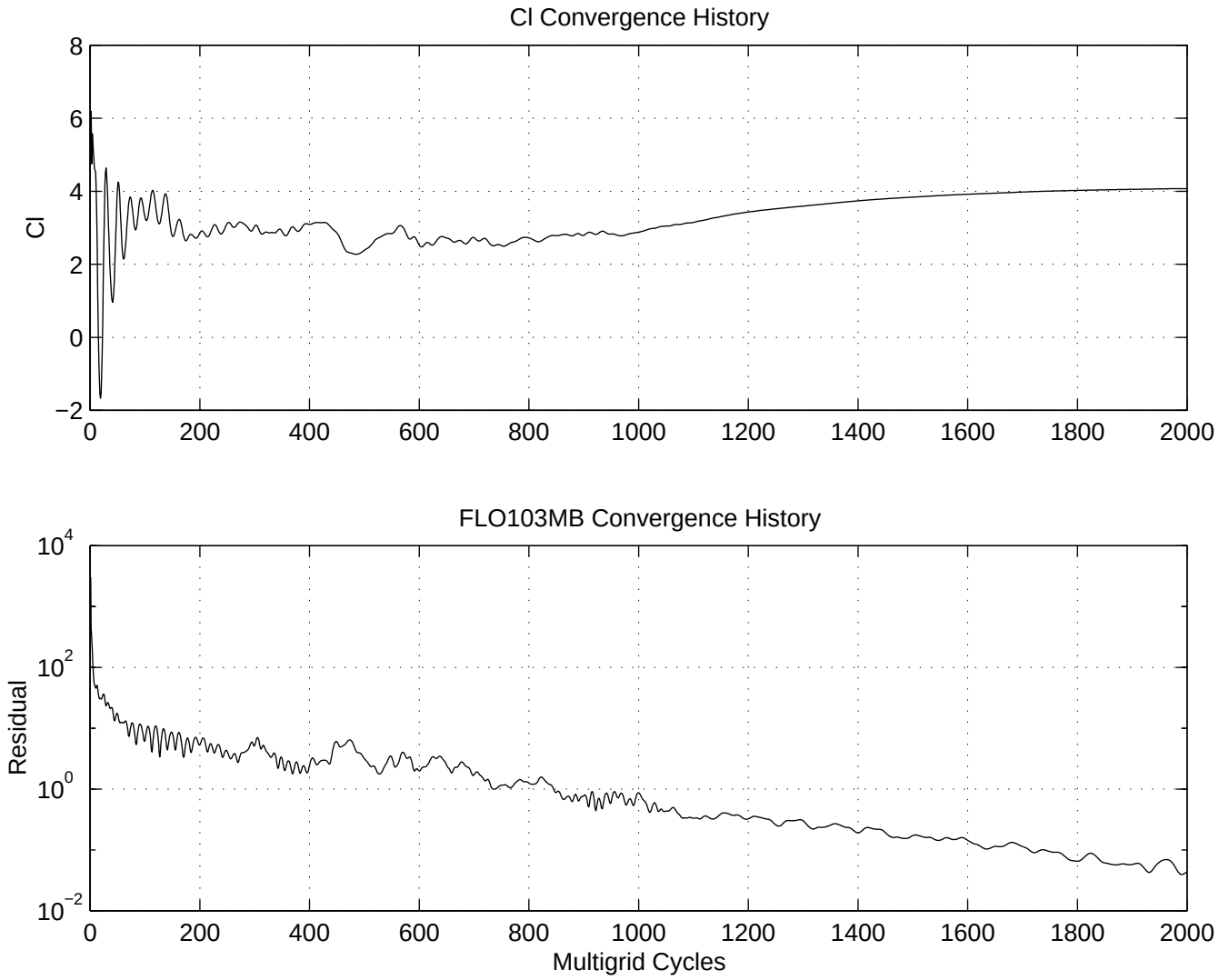

Figure 7: Convergence history of C_l and density residual for the 30P30N multi-element airfoil using the Spalart-Allmaras turbulence model. $M_\infty = 0.20$, $\alpha = 16.02^\circ$, $Re = 9 \times 10^6$.

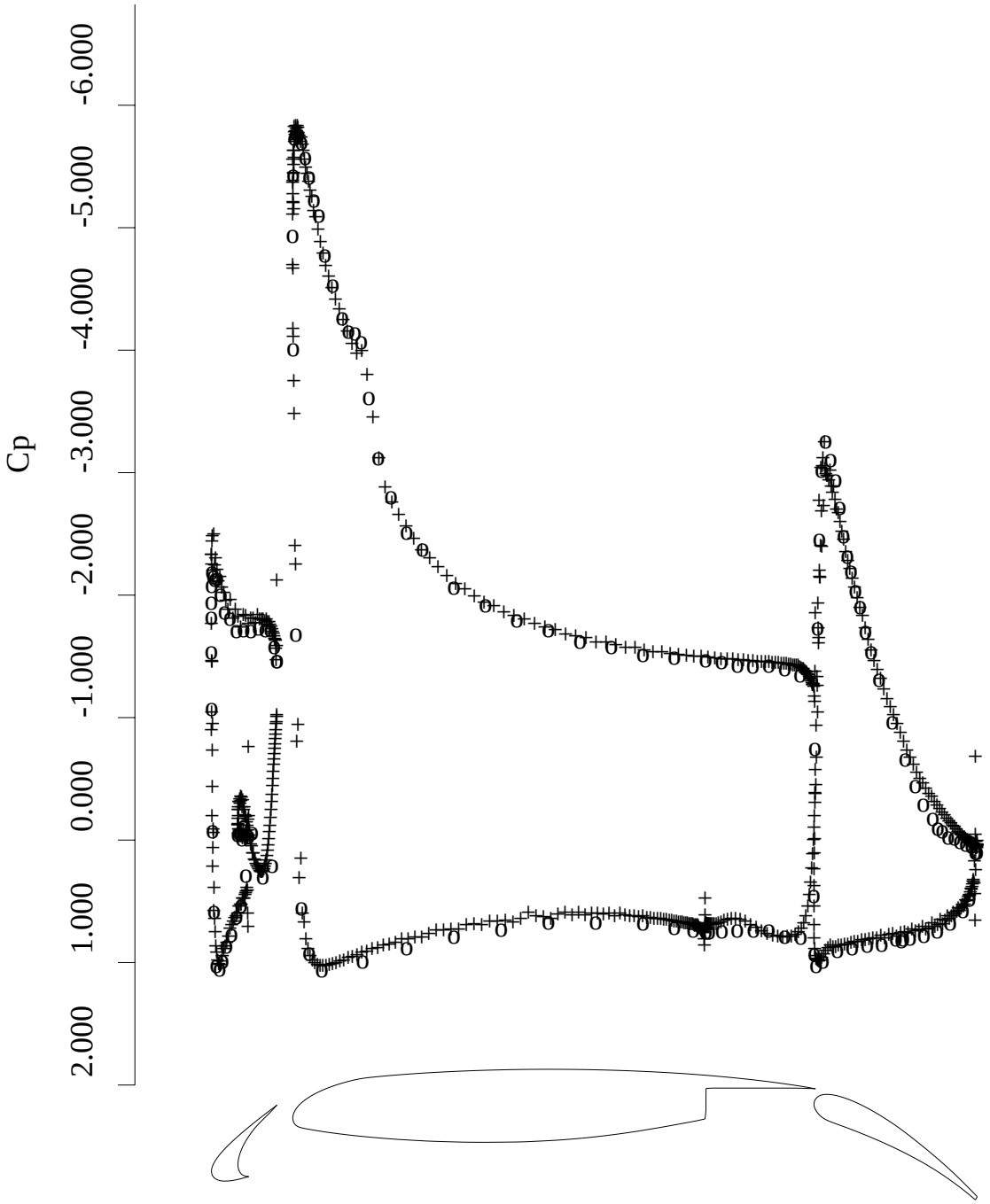

Figure 8: Comparison of experimental and computational pressure coeffient distributions for the 30P30N multi-element airfoil. $M_\infty = 0.20$, $\alpha = 8°$, $Re = 9 \times 10^6$. $+$ Computational C_p, $\circ$ experimental C_p.

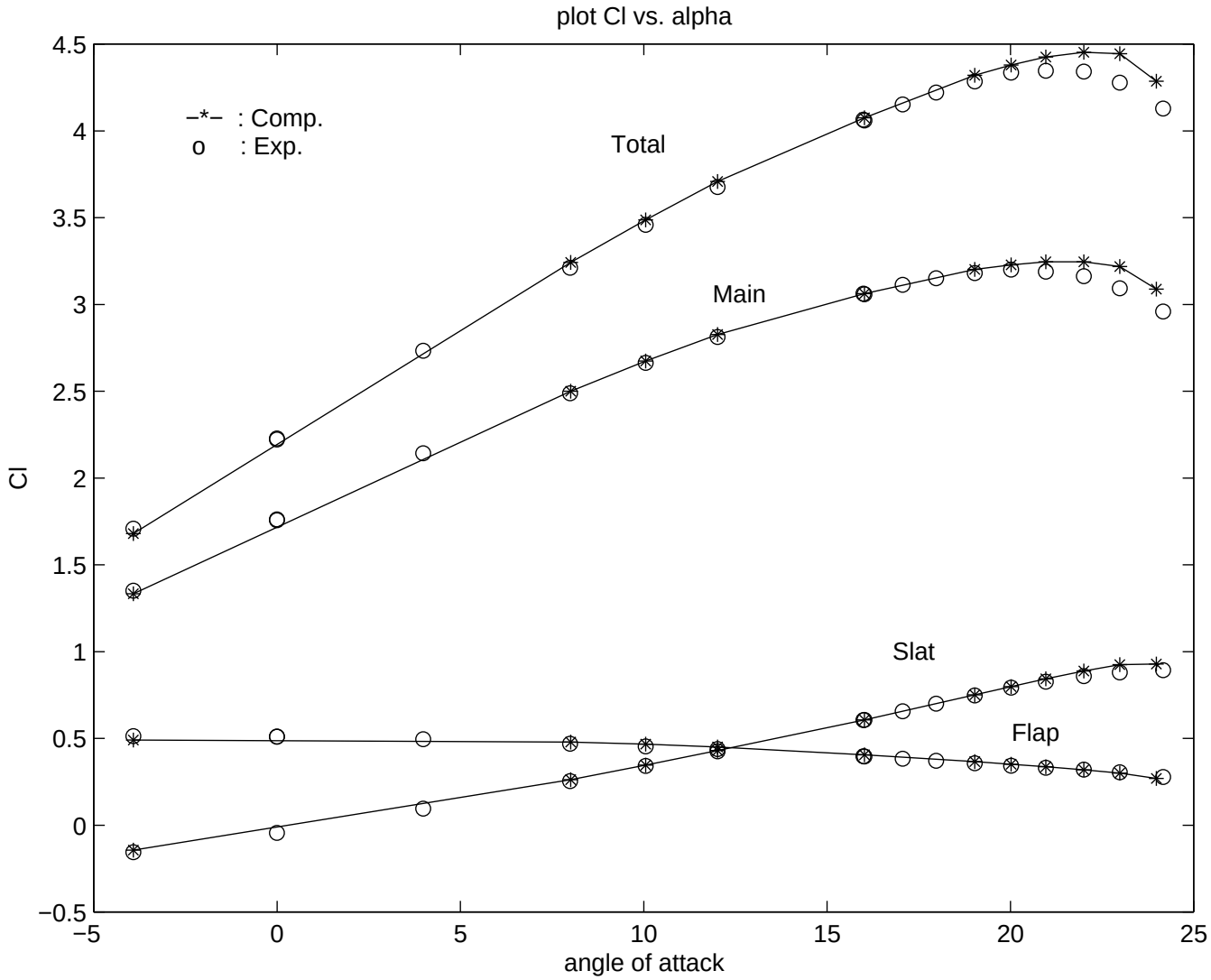

Figure 9: Comparison of experimental and computational lift coeffient vs. angle of attack for the 30P30N multi-element airfoil. $M_\infty = 0.20$, $Re = 9 \times 10^6$. + Computational C_l, $\circ$ experimental C_l.

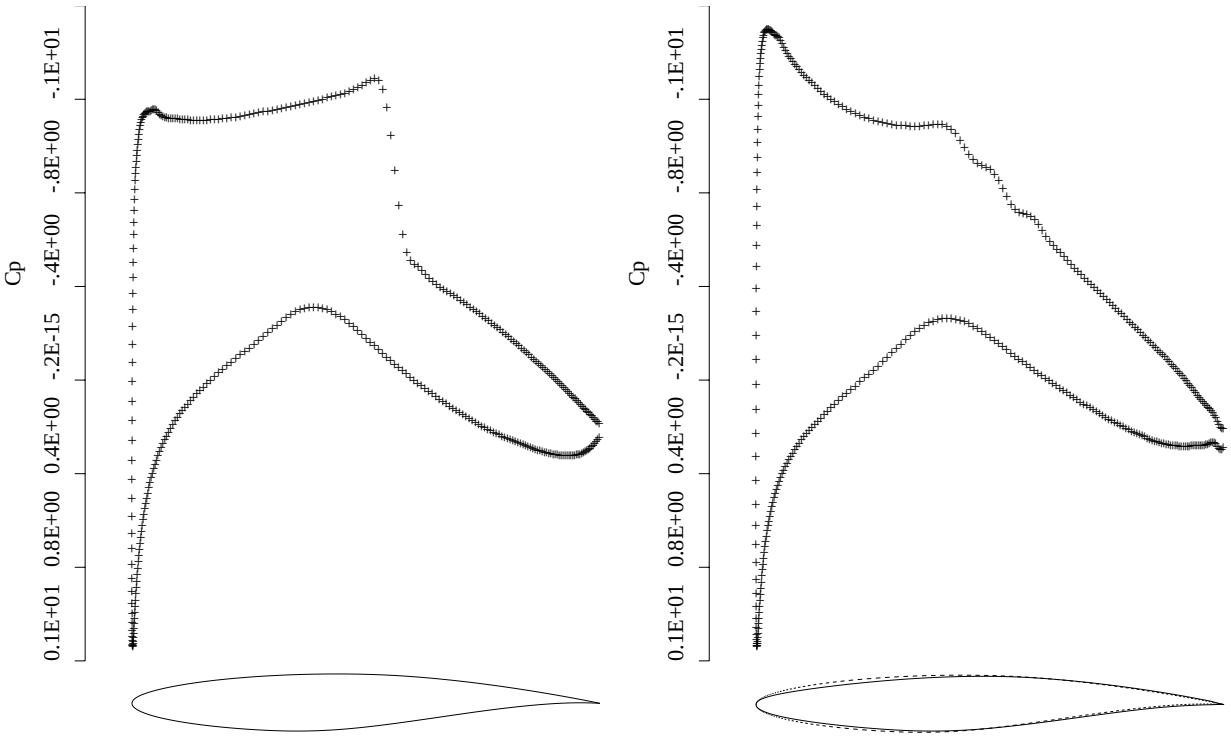

10a: Initial, $C_d = 0.0167$, $M_\infty = 0.73$, $\alpha = 2.977°$, $C_l = 0.8243$, $Re = 6.5 \times 10^6$.

10b: 50 iterations, $C_d = 0.0109$, $M_\infty = 0.73$, $\alpha = 3.172°$, $C_l = 0.8305$, $Re = 6.5 \times 10^6$.

Figure 10: Typical Navier-Stokes drag minimization calculation at fixed $C_l = 0.83$, RAE 2822 airfoil. $- - -$ Initial airfoil, ——— current airfoil.

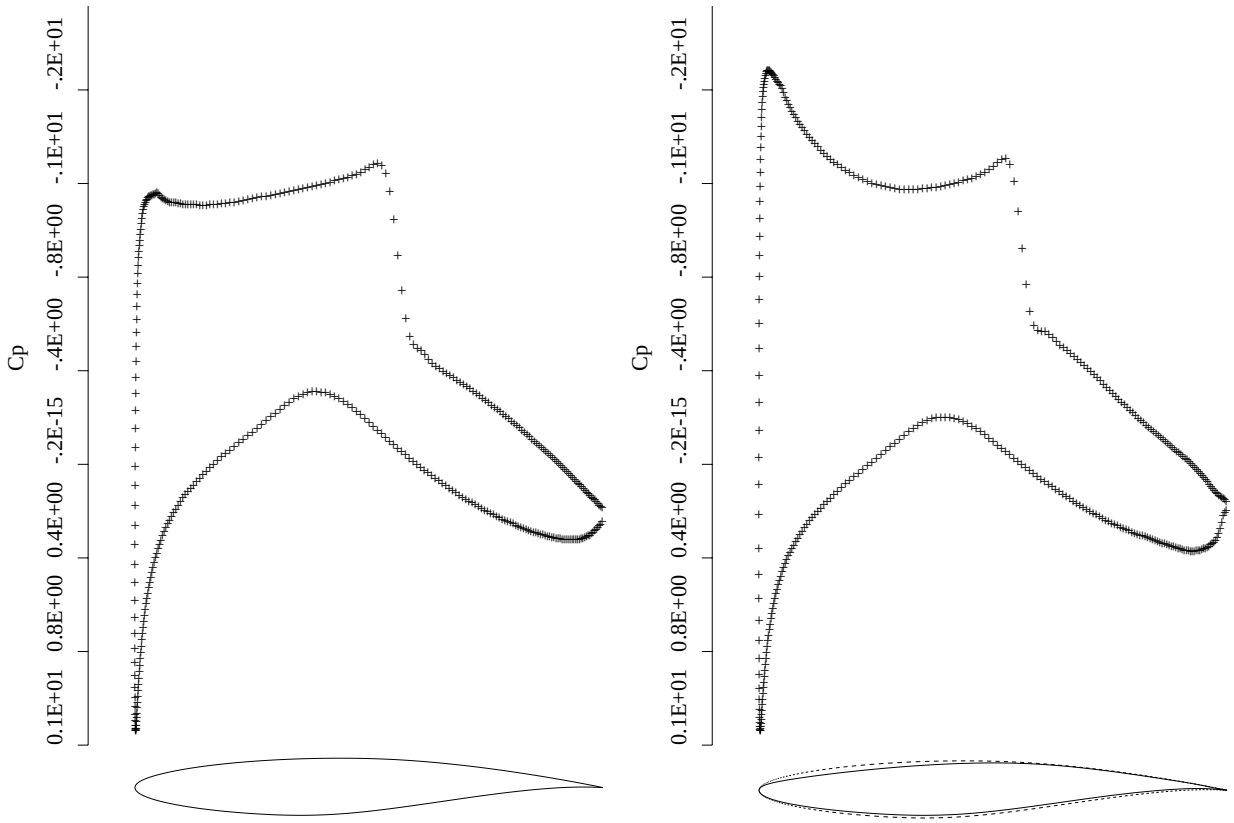

11a: Initial, $C_l = 0.7989$, $M_\infty = 0.73$, $\alpha = 2.794°$, $C_d = 0.0153$, $Re = 6.5 \times 10^6$.

11b: 51 iterations, $C_l = 0.9723$, $M_\infty = 0.73$, $\alpha = 3.355°$, $C_d = 0.0153$, $Re = 6.5 \times 10^6$.

Figure 11: Typical Navier-Stokes lift maximization calculation at fixed $C_d = 0.0153$, RAE 2822 airfoil. $- - -$ Initial airfoil, ——— current airfoil.

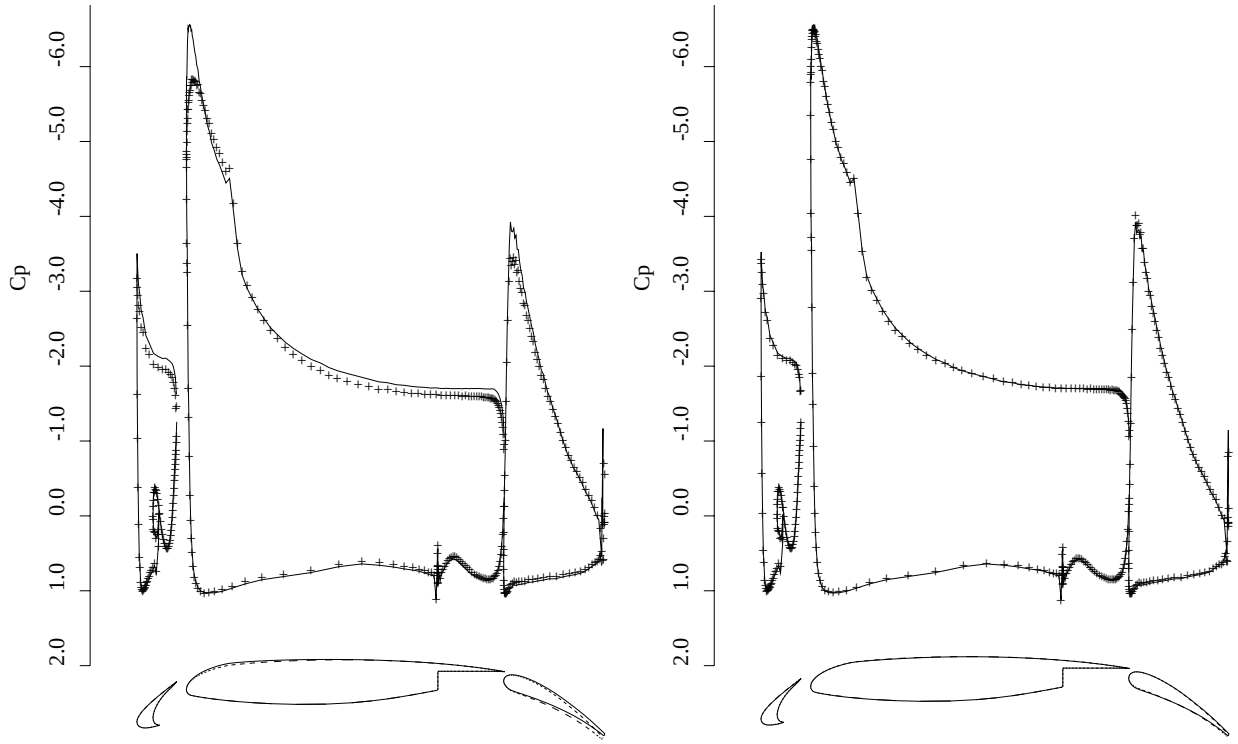

12a: Initial geometry with one bump on the main element and a 2° deflection on the flap.

12b: 100 design iterations using all bumps and rigging variables.

Figure 12: Example of the 30P30N multi-element Euler inverse design. $M_\infty = 0.2$, $\alpha = 8.0^\circ$. $+$ Actual C_p, —— target C_p. $- - -$ Initial airfoil, ——— target airfoil.

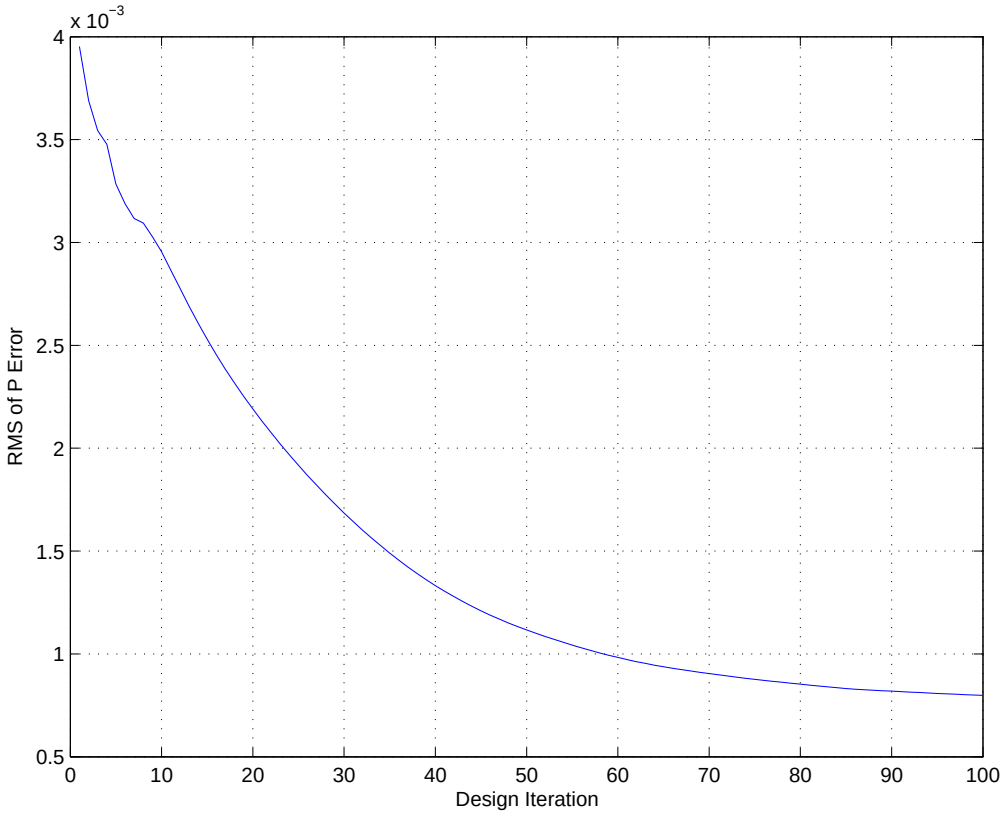

Figure 13: Convergence History of Pressure Difference for the 30P30N multi-element Euler inverse design.

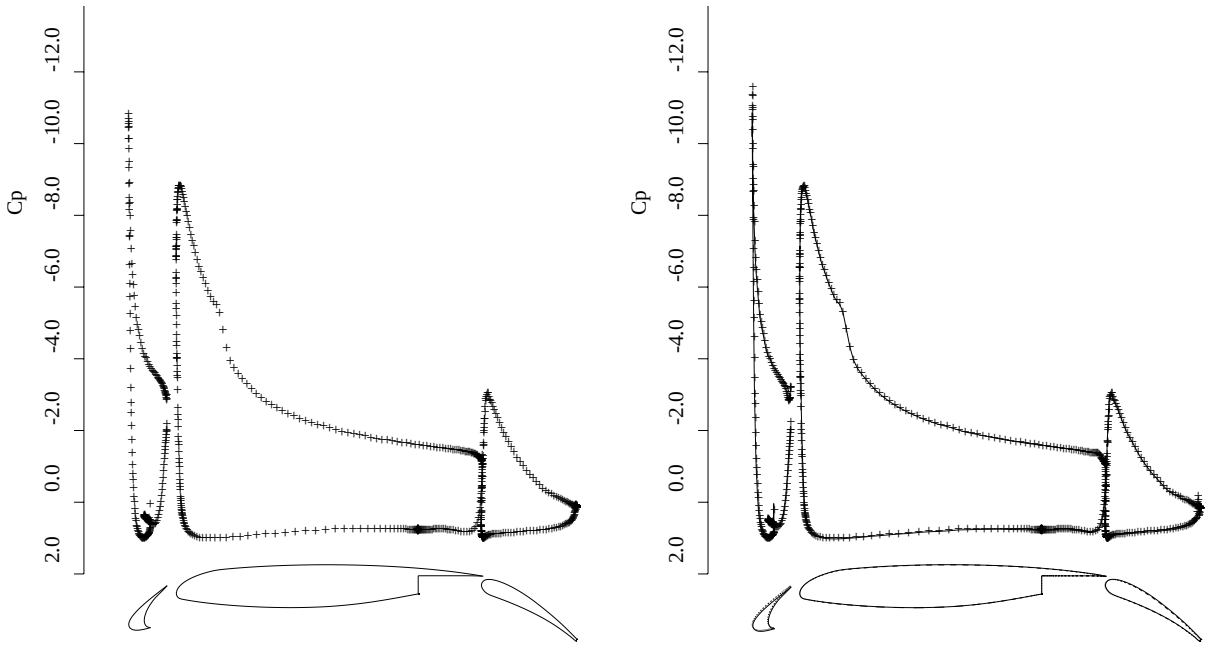

14a: Initial, $C_d = 0.0650$, $M_\infty = 0.2$, $\alpha = 16.02^\circ$, $C_l = 4.0412$, $Re = 9 \times 10^6$.

14b: 9 design iterations, $C_d = 0.0640$, $M_\infty = 0.2$, $\alpha = 16.246^\circ$, $C_l = 4.0478$, $Re = 9 \times 10^6$.

Figure 14: Multi-element airfoil drag minimization calculation at fixed C_l=4.04, 30P30N. $- - -$ Initial airfoil, ——— current airfoil.

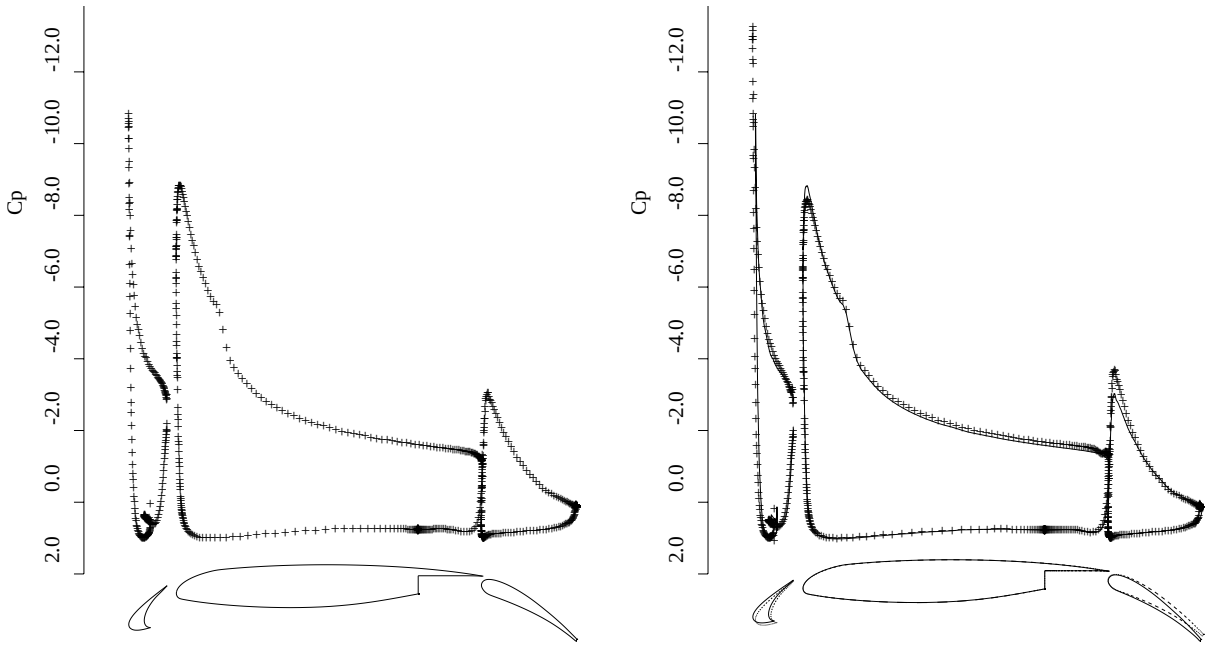

15a: Initial, $C_l = 4.0412$, $M_\infty = 0.2$, $\alpha = 16.02^\circ$, $C_d = 0.0650$, $Re = 9 \times 10^6$.

15b: 19 design iterations, $C_l = 4.1881$, $M_\infty = 0.2$, $\alpha = 16.02^\circ$, $C_d = 0.0697$, $Re = 9 \times 10^6$.

Figure 15: Multi-element airfoil lift maximization calculation at fixed $\alpha = 16.02^\circ$, 30P30N. + Current C_p, —— initial C_p. ——— Current airfoil, − − − initial airfoil.

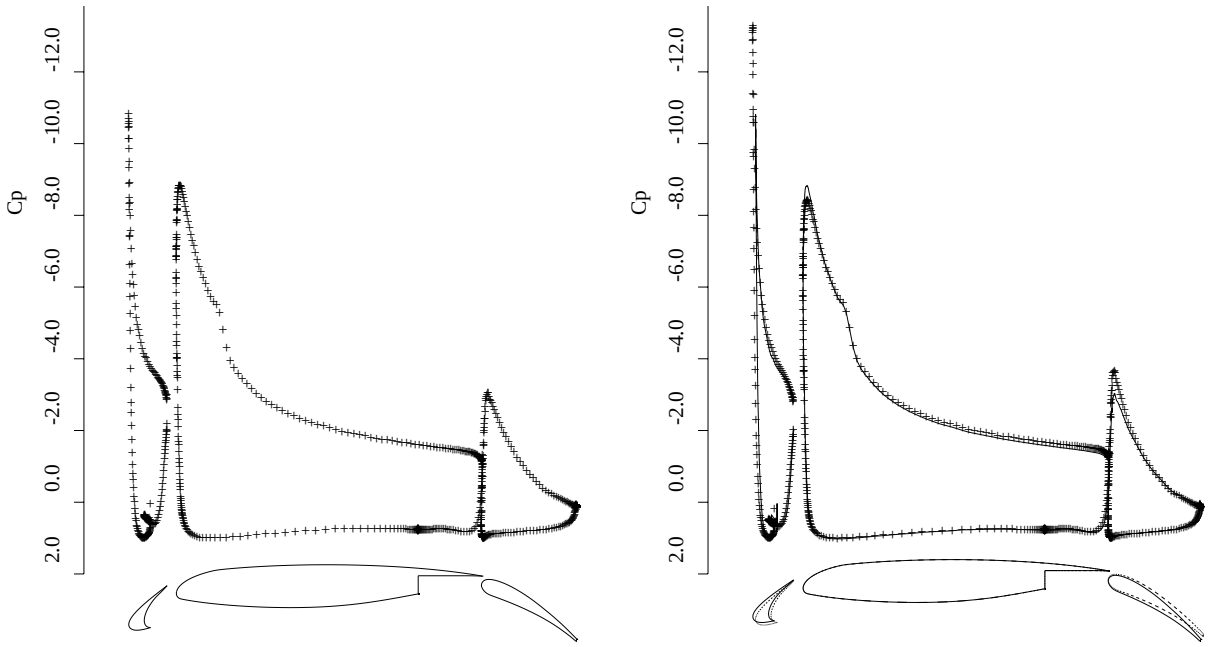

16a: Initial, $C_l = 4.0412$, $M_\infty = 0.2$, $\alpha = 16.02^\circ$, $C_d = 0.0650$.

16b: 19 design iterations, $C_l = 4.1698$, $M_\infty = 0.2$, $\alpha = 16.02^\circ$, $C_d = 0.0689$.

Figure 16: Multi-element airfoil lift maximization using settings only at fixed $\alpha = 16.02^\circ$, 30P30N. + Current C_p, —— initial C_p. ——— Current airfoil, $- - -$ initial airfoil.

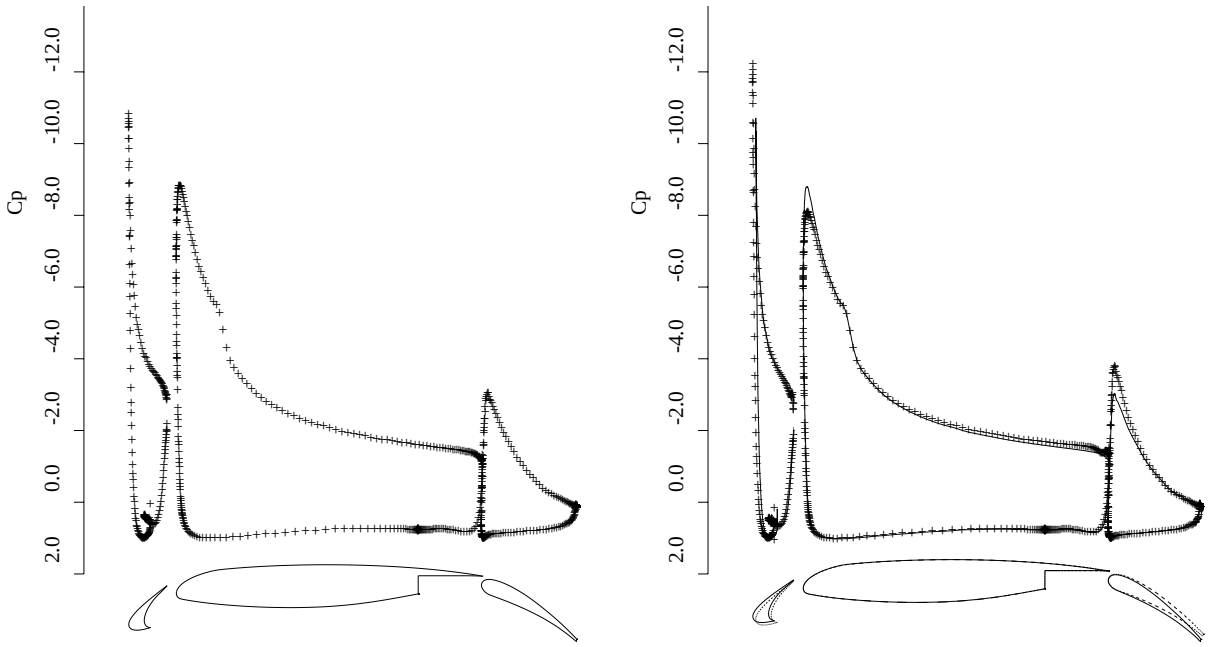

17a: Initial, $C_l = 4.0412$, $M_\infty = 0.2$, $\alpha = 16.02^\circ$, $C_d = 0.0650$.

17b: 10 design iterations, $C_l = 4.1227$, $M_\infty = 0.2$, $\alpha = 15.127^\circ$, $C_d = 0.0661$.

Figure 17: Multi-element airfoil lift maximization calculation at fixed $C_d = 0.0650$, 30P30N. + Current C_p, —— initial C_p. ——— Current airfoil, − − − initial airfoil.

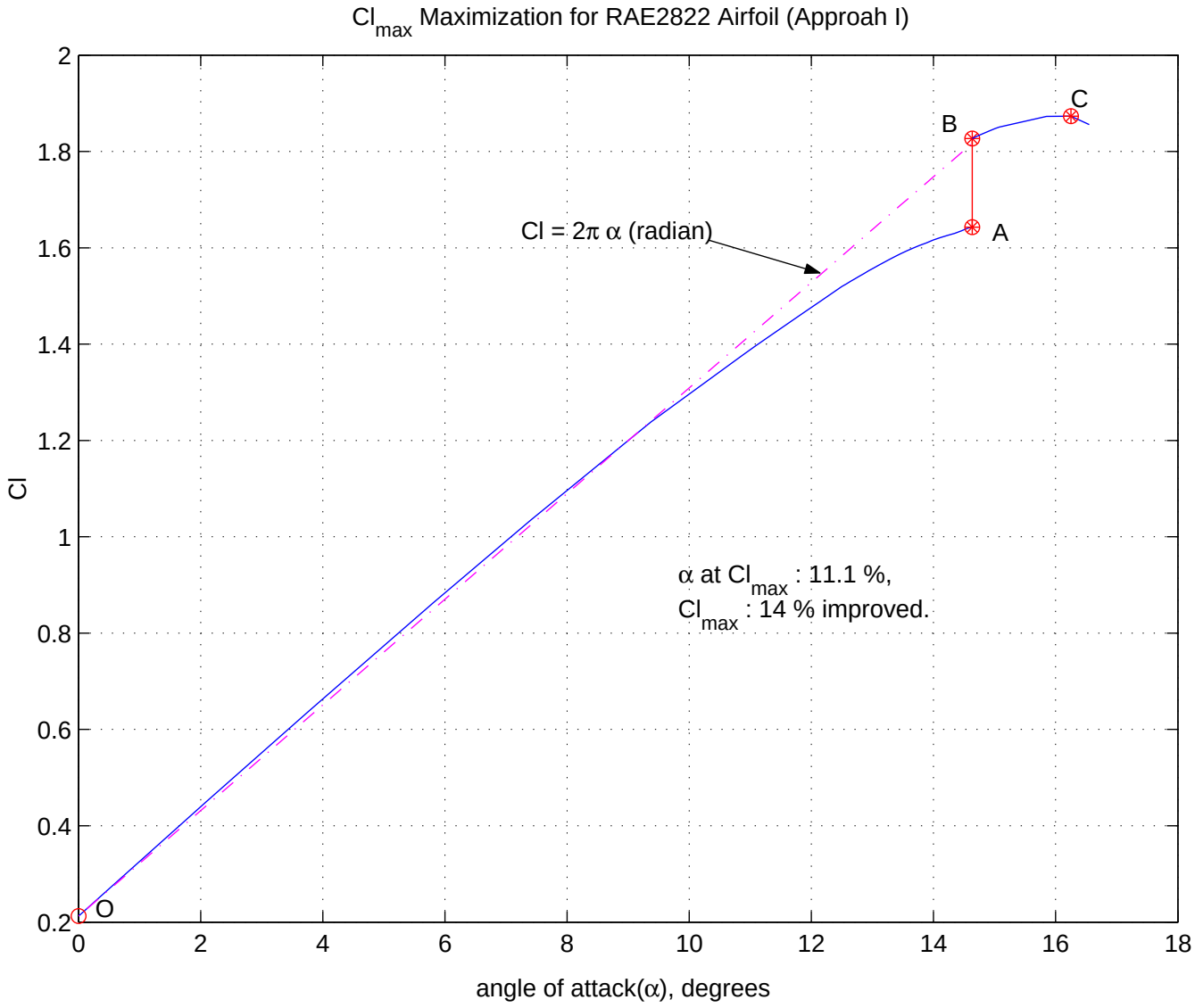

Figure 18: Design curve of approach I for the RAE2822 $C_{l_{max}}$ maximization. $M_\infty = 0.20$, $Re = 6.5 \times 10^6$. O-A: Cl vs. α curve of baseline, A-B: design curve using bumps, B-C: Cl vs. α curve of designed airfoil.

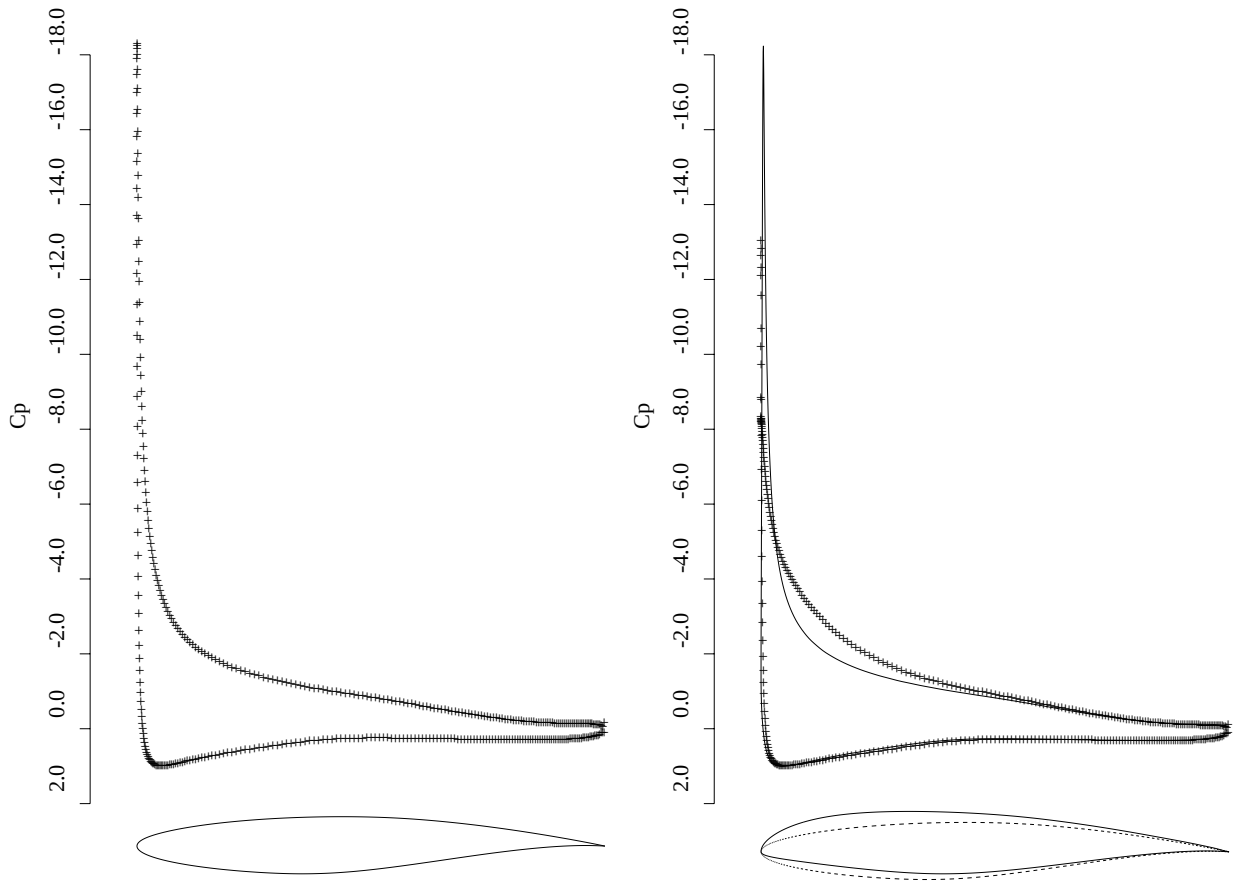

19a: Initial, C_l=1.6430, $M_\infty = 0.2$, $\alpha = 14.633°$, $Re = 6.5 \times 10^6$, $C_d = 0.0359$.

19b: 31 iterations, $C_l = 1.8270$, $M_\infty = 0.2$, $\alpha = 14.633°$, $Re = 6.5 \times 10^6$, $C_d = 0.0326$.

Figure 19: RAE2822 $C_{l_{max}}$ maximization calculation at a fixed $\alpha = 14.633°$. + Current C_p, —— initial C_p. ——— Current airfoil, − − − initial airfoil.

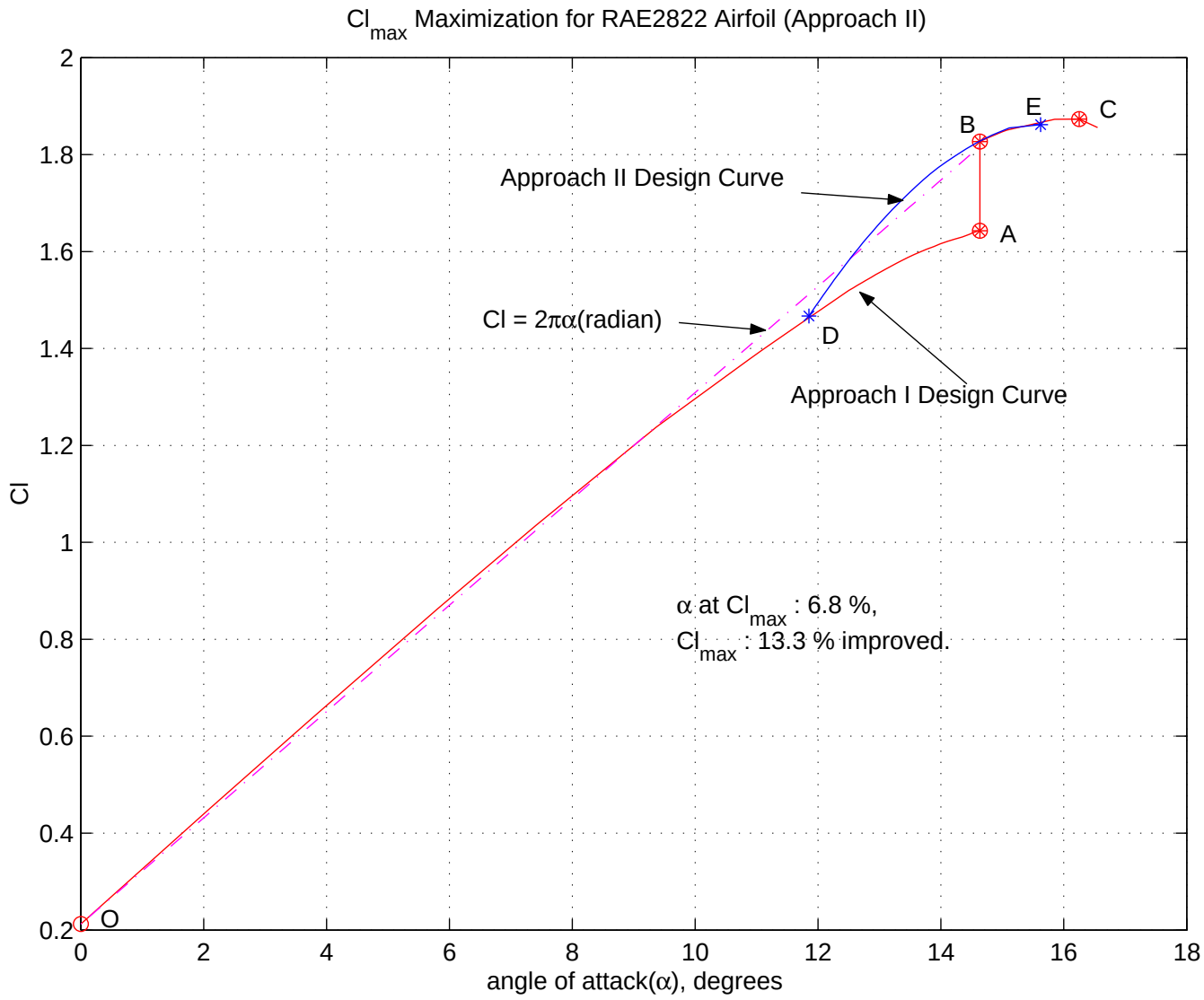

Figure 20: Design curve of approach II for the RAE2822 Cl_{max} maximization. $M_\infty = 0.20$, $Re = 6.5 \times 10^6$. D-E: Approach II design curve.

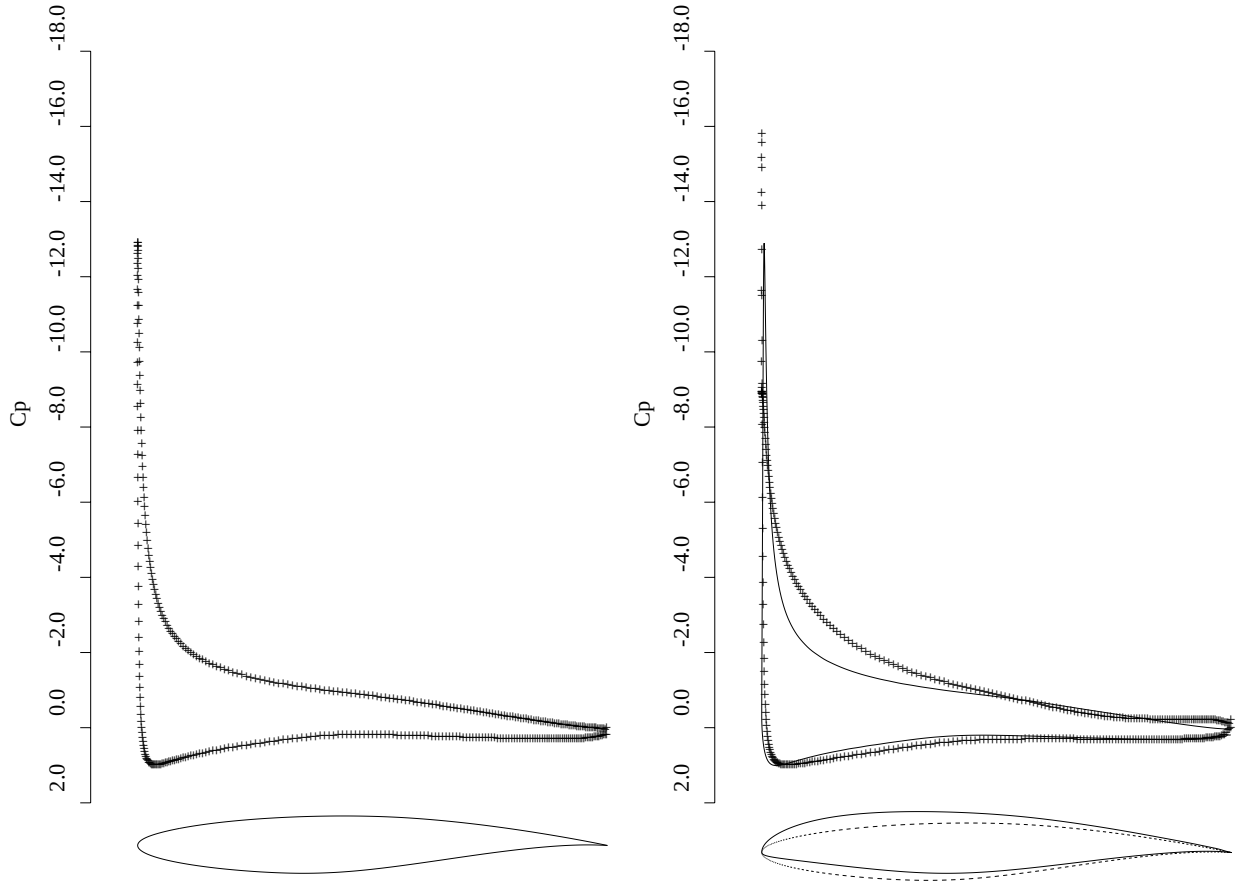

21a: Initial, C_l=1.447, $M_\infty = 0.2$, $\alpha = 11.850°$, $Re = 6.5 \times 10^6$, $C_d = 0.0215$.

21b: 35 iterations, $C_l = 1.8617$, $M_\infty = 0.2$, $\alpha = 15.623°$, $Re = 6.5 \times 10^6$, $C_d = 0.0417$.

Figure 21: RAE2822 $C_{l_{max}}$ maximization calculation including α as a design variable. + Current C_p, —— Initial C_p. ——— Current Airfoil, − − − Initial Airfoil.

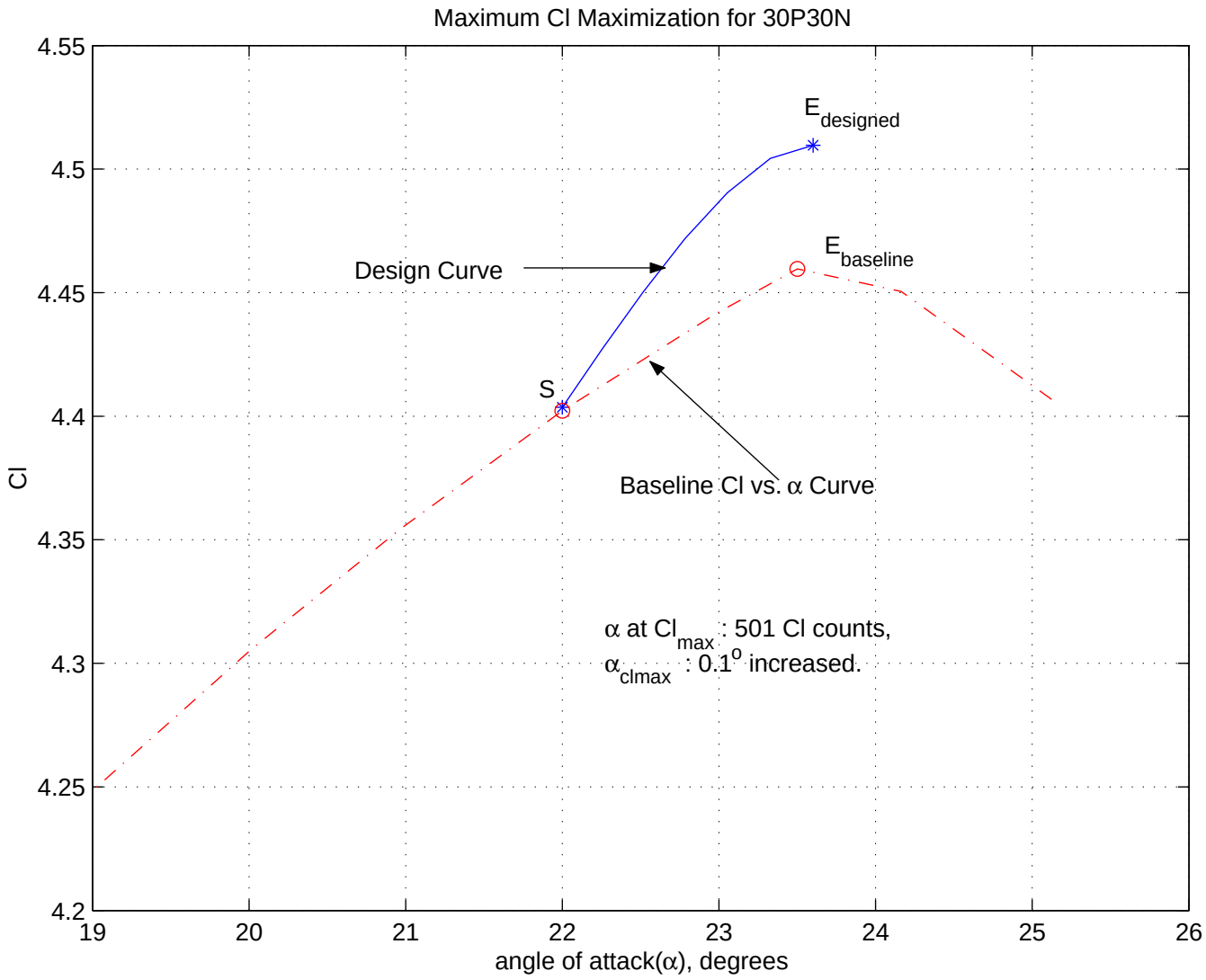

Figure 22: Design curve of the 30P30N $C_{l_{max}}$ maximization. $M_\infty = 0.20$, $Re = 9 \times 10^6$.

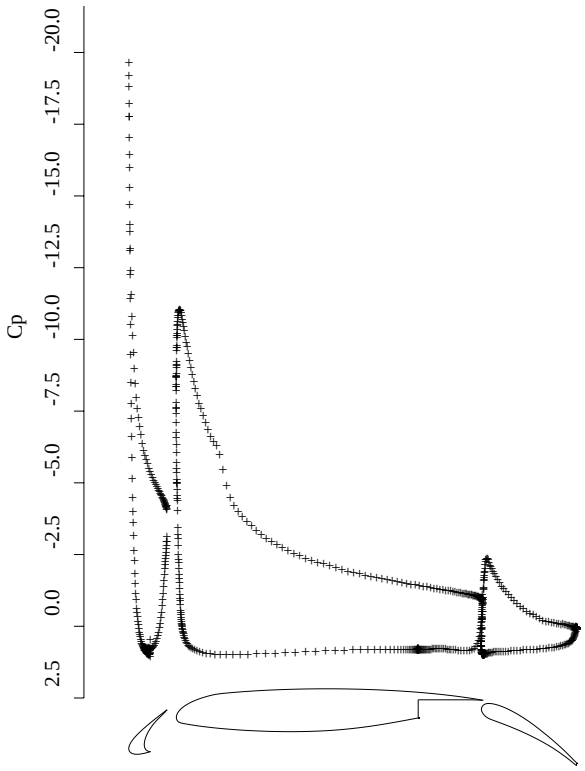

23a: Baseline, $C_l = 4.4596$, $M_\infty = 0.2$, $\alpha = 23.5°$, $C_d = 0.1062$.

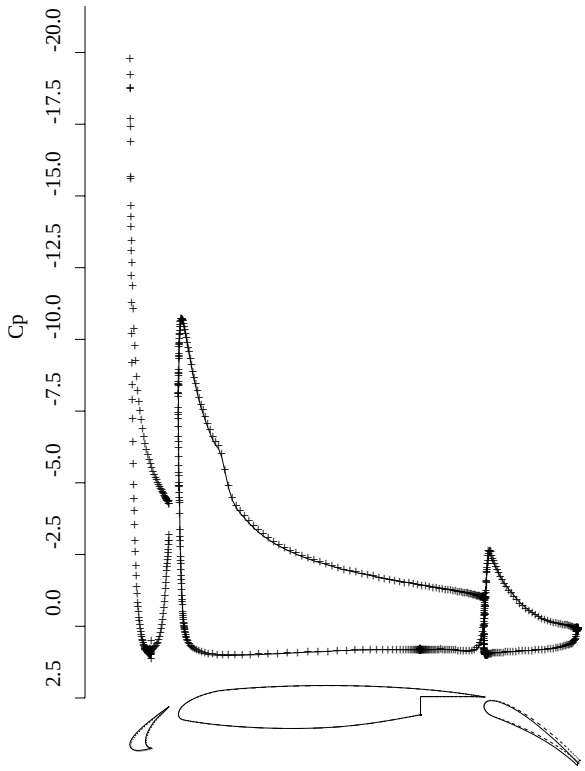

23b: 6 design iterations,$C_l = 4.5097$, $M_\infty = 0.2$, $\alpha = 23.601°$, $C_d = 0.1236$.

Figure 23: Multi-element airfoil $C_{l_{max}}$ maximization calculation for the 30P30N. + Current C_p, —— initial C_p. ——— Current airfoil, − − − initial airfoil.

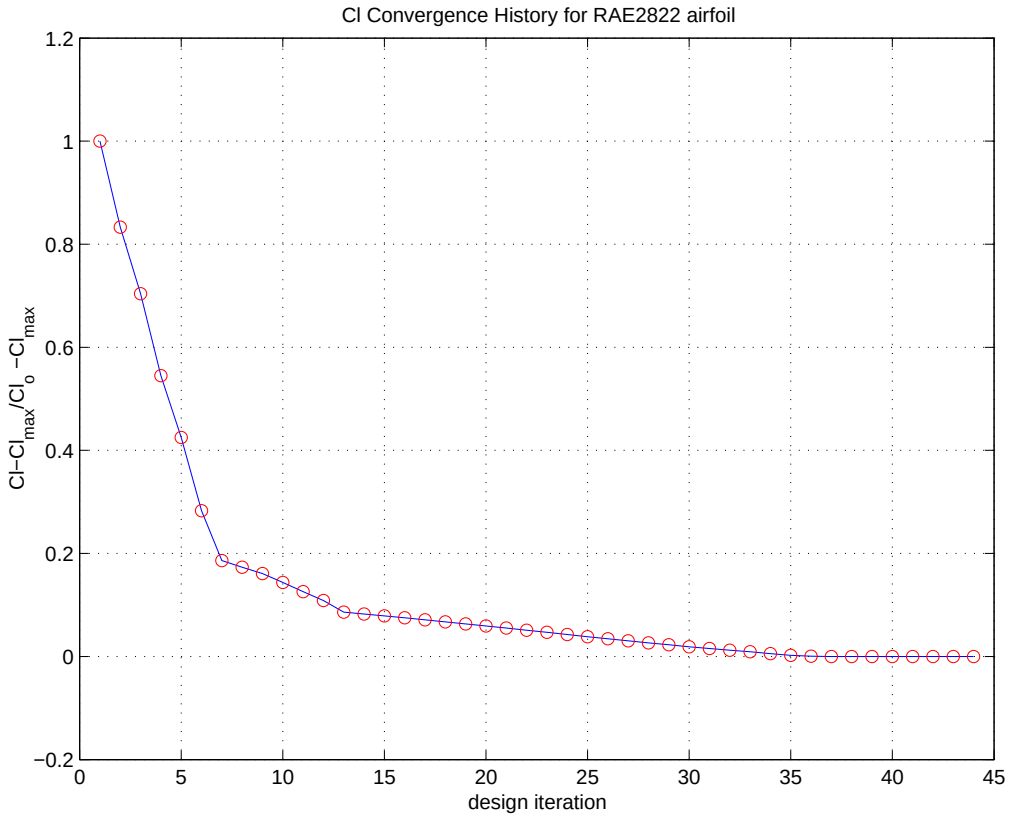

Figure 24: Convergence History for Lift Maximization of RAE2822 Using Angle of Attack as the Only Design Variable.

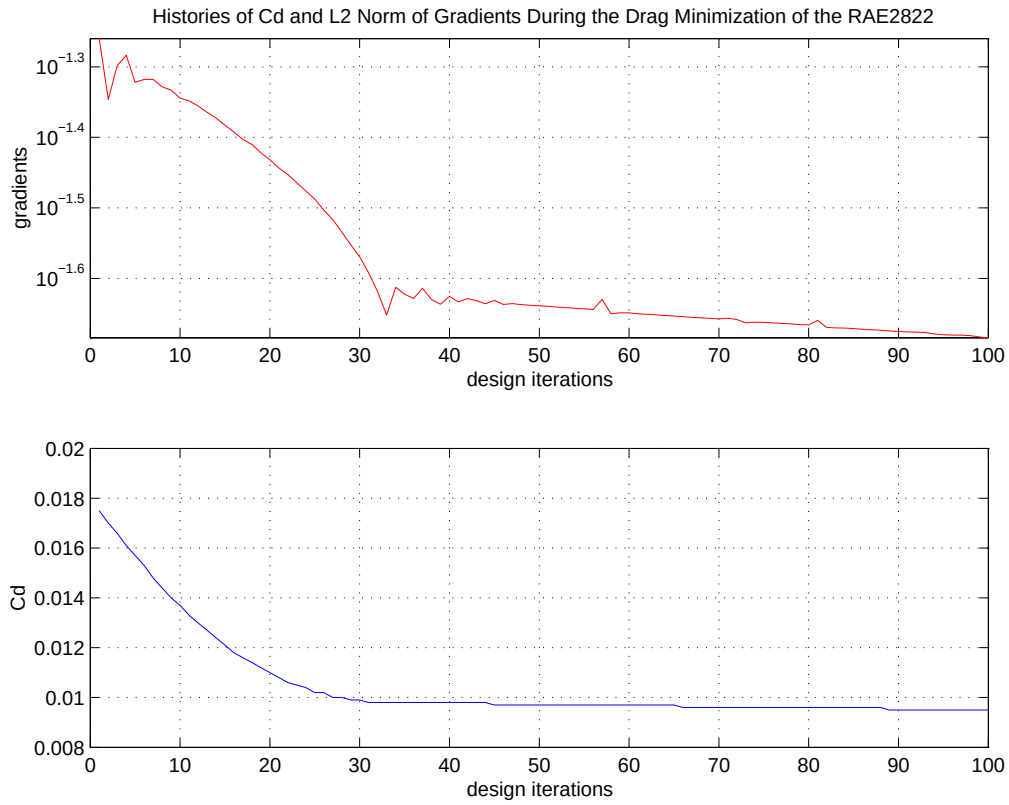

Figure 25: Convergence History for Drag Minimization of RAE2822 at Fixed Angle of Attack.